Applied Catalysis B: Environment and Energy 350 (2024) 123906

Contents lists available at ScienceDirect

Applied Catalysis B: Environment and Energy

journal homepage: www.elsevier.com/locate/apcatb

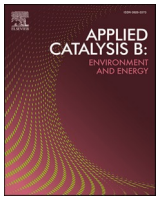

Deciphering the role of nano-CeO_2 morphology on the dry reforming of methane over Ni/CeO_2 using transient and isotopic techniques

Michalis A. Vasiliades [a,1], Constantinos M. Damaskinos [a,1], Maria Lykaki [b], Sofia Stefa [b,c], Vassilios D. Binas [c], Theocharis Kentri [d,e], Soghomon Boghosian [d,e,f], Michalis Konsolakis [b], Angelos M. Efstathiou [a,*]

[a] Department of Chemistry, Heterogeneous Catalysis Laboratory, University of Cyprus, Nicosia, CY, Cyprus
[b] School of Production Engineering and Management, Technical University of Crete, Chania, GR, Greece
[c] Institute of Electronic Structure and Laser, Foundation for Research and Technology, Heraklion, GR, Greece
[d] Department of Chemical Engineering, University of Patras, Patras, GR, Greece
[e] Institute of Chemical Engineering Sciences, FORTH/ICE-HT, Patras, GR, Greece
[f] School of Science and Technology, Hellenic Open University, Patras, GR 26335, Greece

ARTICLE INFO

Keywords:
Dry reforming of methane
Ni supported on CeO_2 nanorods
Oxygen mobility
Oxygen isotopic studies
Transient kinetic studies

ABSTRACT

The effect of ceria morphology, nanorods-NR and nanopolyhedra-NP on important kinetic parameters of the dry reforming of methane (DRM) over Ni/nano-ceria (d_{Ni} ~20 nm) was investigated by transient and isotopic experiments. Transient isothermal reduction by hydrogen evidenced lower activation energy and higher reduction rates of lattice oxygen in the case of CeO_2-NR compared to those of CeO_2-NP. Transient $^{16}O/^{18}O$ isotopic exchange provided a lower E_{app} of bulk oxygen diffusion (by ~90 kJ mol^{-1}) for CeO_2-NR compared to CeO_2-NP. $^{18}O/^{16}O$ isotopic exchange followed by DRM revealed higher carbon oxidation rates by lattice oxygen to $C^{18}O(g)$ in the case of CeO_2-NR compared to those of CeO_2-NP, in harmony with the lower amount of carbon accumulated in the former catalyst. The lower E_{app} of DRM and carbon oxidation by lattice oxygen confirm the higher DRM activity on Ni/CeO_2-NR compared to Ni/CeO_2-NP. HAADF-STEM and Raman studies were linked to the observed transient kinetic results.

1. Introduction

Catalytic dry reforming of methane (DRM; $CH_4 + CO_2 \leftrightarrow 2CO + 2\,H_2$, $\Delta H^{o}_{298K} = +247.3\ kJ\ mol^{-1}$) has gained increasing attention in recent years as an attractive solution not only to suppress global warming (utilization of two major greenhouse gases) but also as an opportunity for the development of "carbon industry" [1]. The latter relates to the production of green H_2 as well as syngas (CO/H_2) that can be subsequently converted into liquid fuels and value-added chemicals, such as methanol, oxygenated compounds and long-chain hydrocarbons [2–4]. Despite the significance of DRM in relation to global warming mitigation and syngas production, its industrial application has not been made feasible yet because of unacceptable catalyst deactivation rates mainly due to carbon deposition and metal sintering [5–8].

Although noble metal-based (e.g. Pt, Ru, Rh, Pd, Ir) supported catalysts are highly active and relatively stable for the DRM reaction, the high cost and availability prohibit their industrial application [7]. The development of low-cost and carbon-free catalytic materials is therefore of paramount importance for DRM industrialization. In this context, nickel-based supported catalysts have been extensively investigated [9–21]. However, coke deposition still remains the main drawback of this class of catalytic materials due to methane decomposition (Eq. (1)) and CO disproportionation (Eq. (2)) reactions [21–23].

$$CH_4 + s \rightarrow 2H_2 + C - s \quad \left(\Delta H^{o}_{298K} = +75\ kJ\ mol^{-1}\right) \tag{1}$$

$$2\,CO + s \leftrightarrow CO_2 + C - s \quad \left(\Delta H^{o}_{298K} = -172\ kJ\ mol^{-1}\right) \tag{2}$$

Suppression of deposited carbon during DRM and its oxidation on ceria-based supported metal catalysts was focused on various strategic approaches, namely: the fine-tuning of active metal size (nanometer

* Corresponding author.
E-mail address: efstath@ucy.ac.cy (A.M. Efstathiou).
[1] Equally contributed

https://doi.org/10.1016/j.apcatb.2024.123906
Received 27 December 2023; Received in revised form 12 February 2024; Accepted 29 February 2024
Available online 2 March 2024
0926-3373/© 2024 Elsevier B.V. All rights reserved.

scale) [14,24,25], the shape of support (e.g., rod, cube, polyhedron) [26–30], and support chemical composition (metal oxides, use of dopants and/or promoters) [16,21,31–33].

CeO_2 has been extensively studied at the fundamental and nanoscale level to understand its functioning as catalyst, support and promoter [34]. This is due to its unique properties for protecting metal particles from sintering and transferring oxygen to the supported metal nanoparticles (oxygen mobility and reducibility), which is driven by the formation of oxygen vacancies and structural defects (Ce^{3+}/Ce^{4+} redox couple) [35–38]. By combining ceria as carrier of various transition metals, novel formulations (doped/promoted ceria) with remarkable catalytic properties can be obtained largely due to the development of metal-support interactions with synergetic effects [7,11,14,39–48]. Therefore, it is very important to engineer metal-support interactions in order to facilitate activation of both CH_4 and CO_2 reactants and at the same time to minimize carbon deposition. For the latter, in the case of Ni/La_2O_3 the basic sites of support assist CO_2 activation and at the same time oxidation of carbon formed on Ni following CH_4 decomposition [7]. Also, it was postulated that activation of CH_4 requires the presence of -OH (acidic supports) or carbonates (basic supports) [7]. Low-temperature DRM on model Ni/CeO_2 catalytic surfaces revealed that for low Ni loadings, ceria can stabilize oxidic $Ni^{\delta+}$ cations at the interface able to lower the energy barrier for C-H bond cleavage [11].

The size, shape and face engineering at the nanometer level has gained particular attention as a tuning tool for adjusting the local surface chemistry, and in turn the catalytic efficiency of metal oxides, including ceria [34,38,39,42,46,49]. In this context, we have recently shown that catalytic materials of high activity, selectivity and stability for various energy and environmental applications can be obtained through size and shape engineering [50–61]. For instance, it has been disclosed through both ex-situ and in-situ techniques that ceria nanorods exposing (100) and (110) crystal facets exhibit superior oxygen mobility and abundance in structural defects [51,53–58], offering extremely active CeO_2-based transition metal catalysts, such as Cu/CeO_2 for CO oxidation [56], and Ni/CeO_2 for CO_2 hydrogenation to methane [53]. Regarding the DRM reaction, Efstathiou and co-workers [25,62–66] have illustrated by advanced transient and isotopic techniques that carbon derived from CH_4 activation can be effectively oxidized by labile oxygen of highly reducible doped-CeO_2 supports, demonstrating the key role of support lattice oxygen in largely reducing carbon deposition. Additionally, Lyu et al. [22] have shown that the concentration of active surface oxygen species can be used as a coke resistance descriptor parameter. Given the key role of labile oxygen species and support reducibility on the DRM reaction, nickel catalysts supported on highly reducible ceria-based carriers have been extensively studied [21,23,25,62–66]. For instance, Ni/CeO_2-Al_2O_3 and Ni/Al_2O_3 were examined for the DRM with the ceria-alumina catalysts exhibiting high coke resistance attributed mainly to the Ni-CeO_2 interactions developed [67]. Moreover, the pivotal role of Ni particle size (20–45 nm in size) on the carbon pathways (CH_4 and CO_2 activation routes) of a $Ni/Ce_{0.8}Ti_{0.2}O_{2-\delta}$ catalyst was recently explored by Efstathiou and co-workers [25] through various transient and isotopic experiments. It was illustrated that $Ni/Ce_{0.8}Ti_{0.2}O_{2-\delta}$ with a Ni particle size of ca. 20 nm exhibits optimum DRM performance at 750 °C in terms of activity and stability due to a lower rate of carbon accumulation. It should be noted that even though the rate of carbon deposition via CH_4 decomposition was found to increase with Ni particle size, the rate of carbon oxidation by the lattice oxygen of support was found to increase by a larger extent with decreasing Ni particle size [25].

Recently, Lorber et al. [68] have shown that Ni crystallites of ~1 nm in size dispersed on ceria nanorods exhibit remarkable DRM activity and stability in comparison to ceria nanocubes and nanospheres. This was mainly ascribed to the presence of highly dispersed Ni for CH_4 activation in conjunction to the high reducibility of ceria towards CO_2 activation. In addition, methane activation and DRM performance were examined on Ni-CeO_2(111), revealing the key role of Ni coverage (ML) towards methane dissociation and DRM process rates. It was shown that the active sites are highly cationic nickel clusters formed at the step edges of ceria, with the highest nickel chemical potential [69]. Moreover, the adsorption and activation of CO_2 can be tailored by surface basicity since a controlled population of basic sites can lead to high activity for both the CO_2 hydrogenation and reforming processes [70].

Motivated by the key role of ceria support morphology on its reducibility and oxygen mobility, the aim of this work is to provide intrinsic kinetic reasons and fundamental insight for the dependence of the rate of carbon accumulation (formation versus removal rate) and kinetic rate of DRM over Ni/CeO_2 on the morphology (shape) of nanoceria support. Towards this goal, various transient kinetic and isotopic experiments (use of $^{18}O_2$) were designed and performed over Ni/CeO_2 of distinct morphology for the first time to the best of our knowledge. Fundamental information related to the following issues was obtained:

(i) The dynamic redox behavior of given morphology (*shape*) of CeO_2 support, and estimation of the apparent activation energy (E^s_{app}, kJ mol^{-1}) of surface oxygen reduction via transient isothermal reduction by hydrogen (H_2-TIR);
(ii) The dynamics of surface oxygen diffusion/exchange, and structural differences of oxygen sublattice among a series of ceria materials of different morphology; use of $^{18}O/^{16}O$ transient isothermal isotopic exchange (TIIE) for estimating the activation energy (E_b, kJ mol^{-1}) of bulk oxygen diffusion;
(iii) The dependence on CeO_2 morphology (shape) of the surface basicity, oxygen vacant sites (V_O) concentration, and dynamics of CO_2 dissociation on V_O sites;
(iv) Kinetic rates and the apparent activation energy of CH_4 conversion (E^{CH4}_{app}, kJ mol^{-1}) on the Ni/CeO_2 solids, along with the amount of carbon accumulated and its oxidation features via temperature-programmed oxidation (TPO);
(v) The *quantification* of the extent of participation of lattice oxygen ($O\text{-}_L$) of ceria support in the oxidation of carbon to CO(g), and comparison to that of the oxygen species (O-s) derived from the CO_2 activation route; the E_{app} (kJ mol^{-1}) of CO formation for both reaction paths was obtained.

HAADF-STEM, *in situ* Raman and powder XRD techniques were used to better correlate the structural with the kinetic or catalytic reaction effects as a function of nano-ceria morphology.

2. Experimental

2.1. Materials synthesis

All chemicals used in this work were of analytical reagent grade. Ce $(NO_3)_3{\cdot}6\,H_2O$ (purity 99.5%, ACROS Organics), tetrabutyl titanate (TBOT, purity 97%, Sigma-Aldrich) and $Ni(NO_3)_2{\cdot}6\,H_2O$ (purity 98%, Alfa Aesar) were used as precursors for the preparation of materials. NaOH (purity 98%, Sigma-Aldrich), ethanol (EMSURE MERCK) and NH_3 (25 vol%, Honeywell Fluka) were also employed during the synthesis procedure. Bare ceria nanoparticles of two different morphologies were initially synthesized by the hydrothermal method [56]. For the synthesis of *ceria nanorods* (CeO_2-NR), 2.75 mol NaOH was initially dissolved in 75 mL of double deionized water. Then, 175 mL of aqueous solution of $Ce(NO_3)_3{\cdot}6\,H_2O$ (0.13 M) was added in the above solution under vigorous stirring until the formation of a milky slurry. The product was left for an additional 1 h under stirring. For the synthesis of *ceria nanopolyhedra* (CeO_2-NP), the same procedure as mentioned above was followed with only one variation, namely, the final aging was performed at 180 °C instead of 90 °C. Afterwards, the solid products were recovered by centrifugation. The solid materials were washed thoroughly with doubly deionized water until pH=7 to remove any co-precipitated salts, and then washed with ethanol to avoid agglomeration. The

resulting gel was dried at 120 °C for 17 h, followed by cooling to room T and calcination, initially at 500 °C for 6 h (heating rate, $\beta = 1$ °C min^{-1}) and then at 700 °C for 4 h (heating rate, $\beta = 5$ °C min^{-1}). Details of the synthesis of ceria-supported Ni samples is provided in the Electronic Supporting Information (ESI).

2.2. Materials characterization

2.2.1. Structure and morphology

The bulk structure of the ceria-supported Ni materials was examined by powder X-ray diffraction (pXRD) employing a Rigaku diffractometer (see details in ESI). The mean primary crystallite size of a given crystal phase was calculated by using the Scherrer Eq. (3):

$$d(nm) = \frac{K\lambda(nm)}{B\cos(\theta_B)} \quad (3)$$

where K is the Scherrer constant (shape dependent), λ is the wavelength of the X-rays in nm, B is the line broadening, and θ is the Bragg angle. The mean primary crystallite size of ceria and NiO phases was determined based on the most intense diffraction peak of (111) CeO_2 (2θ/28.5°) and (200) NiO (2θ/44.5°). Considering that Ni and NiO particles preserved similar crystallite geometrical shapes, and after using the mass densities of Ni and NiO bulk phases, the Ni mean particle size was estimated via the following Eq. (4):

$$d_{Ni}\ (nm) = 0.847\ d_{NiO}\ (nm) \quad (4)$$

The surface morphology of the solids was investigated by High Resolution Transmission Electron Microscopy (HR-TEM) analyses (see details in ESI).

In situ Raman spectra were recorded by using a homemade Raman optical furnace, described in detail previously [71,72]. About 120 mg of each sample was pressed into a wafer disc and mounted by means of a gold wire on the sample supporter of the Raman cell. The temperature was controlled by a thermocouple placed inside a sheath in contact with the sample supporter (see further details in ESI). The protocol of Raman measurements was the following. Each sample was brought to 450 °C under 20% O_2/He gas flow (30 NmL min^{-1}) and the *in situ* Raman spectrum was recorded after 1 h. The feed gas was then switched to 5% H_2/He gas flow (50 NmL min^{-1}) for 1.5 h, where the *in situ* Raman spectrum under reducing conditions was recorded. The feed gas was then switched to 20% O_2/He for 30 min, and the *in situ* Raman spectrum under oxidizing conditions was then obtained, where the reinstatement of the initial sample state was confirmed in each case. In order to account for "path length" effects, *i.e.* variations in absorption of the incident laser light by the samples exhibiting different colors, normalization of the Raman spectra was applied [73,74]. Additionally, to focus on inherent structural/vibrational effects, temperature effects (e.g., depopulation of the ground state, Boltzmann distribution) must be accounted for. The temperature effect can be eliminated by the so-called "reduction" procedure of the normalized spectra, which due to the boson-like statistical description of the phonons, the following expression (Eq. (5)) for the reduced normalized Stokes Raman intensity is obtained:

$$I_R^S(\tilde{\nu}) = \frac{\tilde{\nu}}{(\tilde{\nu}_0 - \tilde{\nu})}\left[\frac{1}{\exp(hc\tilde{\nu}/k_BT) - 1}\right]^{-1} I_M^S(\tilde{\nu}) \quad (5)$$

where $I_M^S(\tilde{\nu})$ is the measured normalized Stokes Raman intensity at wavenumber $\tilde{\nu}$, $\tilde{\nu}_0$ is the laser line wavenumber, c is the light velocity, h is the Planck's constant, and k_B is the Boltzmann's constant.

2.2.2. Transient isothermal reduction by hydrogen (H_2-TIR)

Transient isothermal reduction by hydrogen (H_2-TIR) was used to investigate the dynamics of surface and bulk oxygen reduction processes over CeO_2-NP and CeO_2-NR supports as a function of reaction temperature (use of 1 vol% H_2/He gas mixture). Following sample pretreatment (see details in ESI), the step-gas switch from He to 1% H_2/1% Kr/98% He at 600 °C (H_2-TIR, 100 NmL min^{-1}) was made, and the transient response curves of Kr (m/z = 84) and H_2 (m/z = 2) were monitored by mass spectrometer. The obtained features of the dynamic rate response curve of H_2 consumption could be regarded as a fingerprint of the redox behavior of a given structure/morphology of solid. The above-described H_2-TIR experiment was repeated at higher temperatures (ca. 625, 650 and 700 °C). Based on a material balance regarding the H_2 molecular species for a flow-reactor under non-steady-state operation, the *dynamic rate* of oxygen reduction by hydrogen at a given temperature, R_{H2} (T, t) (mol H_2 g^{-1} s^{-1}) was estimated (Eq. (6)). Integration of this dynamic rate provided the specific amount of hydrogen consumed, N_{H2} (mol H_2 g^{-1}), named dynamic oxygen storage capacity (DOSC).

$$R_{H_2}\left(\text{mol } H_2\ g^{-1}\ s^{-1}\right) = \frac{F_T}{W}\left(y_{Kr}(t) - y_{H_2}(t)\right) - \left(\frac{N_T}{W}\right)\frac{dy_{H_2}}{dt} \quad (6)$$

In Eq. (6), F_T is the total molar flow rate (mol s^{-1}) of the hydrogen gas mixture used, W is the amount (g) of solid sample, y_i is the mole fraction of gas (Kr or H_2), and N_T is the total number of mols of gas in the reactor (mols).

The initial dynamic rate of H_2 consumption (maximum rate occurred at very short times) was calculated at each temperature, and an apparent activation energy (E_{app}^s) for surface oxygen reduction was estimated after plotting Ln(R_{H2}) vs 1/T based on the following relationship:

$$R_{H_2} = k_o \exp\left(-E_{app}^s \Big/ RT\right) C_{O-s} P_{H_2} \quad (7)$$

It is reasonable to assume that the surface concentration of lattice oxygen, $C_{O\text{-}s}$ is very similar at the very initial stage of the transient independent of temperature, and the same is true for P_{H2} (small amount of H_2 consumed at the very initial stage of the transient).

2.2.3. $^{16}O/^{18}O$ transient isothermal isotopic exchange ($^{18}O_2$-TIIE)

$^{16}O/^{18}O$ transient isothermal isotopic exchange (TIIE) involved the step-gas concentration switch 2% $^{16}O_2$/He (T, 30 min) → 2% $^{18}O_2$/1% Kr/He (T, t) over the CeO_2 support which was first pre-treated in 20% $^{16}O_2$/He at 700 °C for 2 h, followed by a 30-min treatment in 2 vol% $^{16}O_2$/He gas mixture (100 NmL min^{-1}) at the examined temperature range (600–700 °C). At the switch to the equivalent ^{18}O-containing gas mixture (TIIE), the dynamic gas-phase response curves of $^{16}O_2$, $^{16}O^{18}O$ and $^{18}O_2$ (m/z = 32, 34, and 36, respectively) were recorded using on-line mass spectrometry. After applying appropriate material balances for an open flow-reactor, the transient rates $^{16}O^{18}O$(g) and $^{16}O_2$(g) were estimated (Eqs. (8)-(9)) [75]:

$$R_{^{16}O^{18}O}\left(\text{mol } g^{-1}\ s^{-1}\right) = \frac{F_T}{W}\left(y_{^{16}O^{18}O}(t)\right) - \left(\frac{N_T}{W}\right)\frac{dy_{^{16}O^{18}O}}{dt} \quad (8)$$

$$R^{16}O_2\left(\text{mol } g^{-1}\ s^{-1}\right) = \frac{F_T}{W}\left(y_{O_2}(t) - y_{Kr}(t)\right) - \left(\frac{N_T}{W}\right)\frac{dy_{O_2}}{dt} \quad (9)$$

The rate of total ^{16}O exchanged, R_{16O} (mol ^{16}O g^{-1} s^{-1}) is given by the following Eq. (10):

$$R_{^{16}O}\left(\text{mol } g^{-1}\ s^{-1}\right) = R_{^{16}O^{18}O} + 2R_{^{16}O_2} \quad (10)$$

In Eqs. (8)-(9), F_T is the total molar flow rate (mol s^{-1}) of the feed gas stream, y_i is the mole fraction of i ($^{16}O^{18}O$, $^{16}O_2$) at the outlet of the CSTR microreactor, N_T is the total number of mols in the CSTR microreactor, and W is the amount of sample used (ca. 40 mg). It is noted that the accumulation term in Eqs. (8)-(9) was found negligible compared with the other terms, while in Eq. (8), the input term of $^{16}O^{18}O$ due to the ^{16}O impurity present in the 2 vol% $^{18}O_2$/Kr/Ar gas mixture was negligible compared to the other terms.

The dynamics of the change of ^{18}O fractional composition in the gas

phase (dynamics of surface $^{16}O/^{18}O$ exchange and that in the bulk) was estimated based on the $a_g^{(18)}(t)$ descriptor parameter given by Eq. (11) [75]:

$$a_g^{(18)}(t) = \frac{y_{^{16}O^{18}O} + 2y_{^{18}O_2}}{2\sum y_{i\,O}} \quad (11)$$

where, y_i is the mole fraction of gaseous species i ($^{16}O_2$, $^{16}O^{18}O$ and $^{18}O_2$) at any time after the step-gas oxygen isotopic switch. The bulk oxygen diffusivity, D_b ($cm^2\ s^{-1}$) of the CeO_2 support lattice oxygen was estimated based on the pseudo-steady state rate of $^{16}O^{18}O$ formation (20 min after the isotopic switch) using Eq. (12) [76,77]. The Arrhenius relationship for the diffusivity as a function of temperature ($D_b = D_o \exp(-E_b/RT)$) was used to estimate the apparent activation energy (E_b, kJ mol^{-1}) of bulk lattice oxygen diffusion.

$$D_b\ (cm^2\ s^{-1}) = \pi\, t_{s.s.} \left(\frac{N_A}{C_{A_0}}\right)^2 \quad (12)$$

In Eq. (12), $t_{s.s.}$ (s) is the time that $^{16}O^{18}O$ formation rate reaches its pseudo-steady state, N_A (mol s^{-1} cm^{-2}) is the molar flux of atomic ^{16}O from the bulk to the surface of the solid, and C_{A0} (mol cm^{-3}) is the concentration of atomic oxygen in the bulk. Due to the experimental uncertainty in $t_{s.s.}$, extraction of accurate values of D_b was not possible. However, an accurate estimation of E_b is not influenced by the accuracy in determining the $t_{s.s.}$ parameter (Eq. (12)).

2.2.4. CO_2 chemisorption on oxygen vacant sites followed by temperature-programmed desorption (CO_2-TPD)

The dynamics of CO_2 chemisorption at 700 °C, following H_2 reduction at the same temperature for creating oxygen vacancies in the ceria support was investigated. Upon the completion of CO_2/He gas treatment (no further consumption of CO_2), the ceria sample was cooled in He gas flow to 30 °C, followed by CO_2 chemisorption and temperature-programmed desorption (CO_2-TPD). These studies aimed to investigate how surface basicity, oxygen vacancy (V_O) formation, and CO_2 dissociation on V_O (important steps in the DRM reaction path) are influenced by the CeO_2 morphology (shape). Details of the experimental procedure applied are provided in ESI.

2.3. Steady-state kinetic rates and carbon deposits - DRM reaction

The experimental apparatus used for evaluating the catalytic activity in terms of kinetic rates of the 5 wt% Ni supported on CeO_2-NR and CeO_2-NP carriers, and that used for performing various transient step-gas concentration switches was previously described [78–80]. The fresh catalyst (ca. 0.1 g) after ground and sieved to less than 106 μm in size was well mixed with SiC (1 cat: 2 SiC w/w), and the resulting catalytic bed was used in the 650–700 °C range with a feed gas composition of 20 vol% CH_4/20 vol% CO_2/60 vol% He at 50 NmL min^{-1} and a GHSV of ~ 30,000 ($L_{gas}/L_{cat}/h$). Under these experimental conditions, X_{CH4} and X_{CO2} were kept below 15%. Internal and external mass transport resistances were checked using the experimental procedures described elsewhere [81]. The composition of the effluent gas stream from the reactor was continuously monitored by on-line MS for H_2 ($m/z = 2$), CH_4 ($m/z = 15$), CO ($m/z = 28$), and CO_2 ($m/z = 44$), followed by an infrared gas analyzer (Horiba, Model VA-3000) for CO and CO_2 analysis as well. Calibration of the MS and IR gas analyzers responses was made after using certified calibration gas mixtures (ca. 2% CO/1% CH_4/1% H_2/He and 1% CO_2/He). The kinetic reaction rates for CH_4 and CO_2 conversion and H_2 formation, as well as the H_2/CO gas ratio after 30 min time-on-stream in the DRM reaction were estimated using Eqs. (13)-(16):

$$R_i\ (\text{mol}\ g^{-1}\ s^{-1}) = \frac{F_T^{out}\ y_i^f\ X_i}{W}\ (i = CH_4 \text{ or } CO_2) \quad (13)$$

$$x_i = \frac{F_i^{in} - F_i^{out}}{F_i^{in}} \quad (14)$$

$$R_j\ (\text{mol}\ g^{-1}\ s^{-1}) = \frac{F_T^{out}\ y_j}{W}\ (j = H_2 \text{ or CO}) \quad (15)$$

$$\frac{H_2}{CO} = \frac{R_{H2}}{R_{CO}} \quad (16)$$

where, F_i^{in} and F_i^{out} are the molar flow rates (mol s^{-1}) of reactant i (CH_4 or CO_2) at the inlet and outlet of reactor, respectively, F_T^{out} is the total molar flow rate (mol s^{-1}) at the outlet of reactor, y_j is the mole fraction of component j at the outlet of reactor. The F_i^{out} was estimated based on the measured total volume flow rate at the outlet of reactor (use of soap bubble-meter at room temperature) and the mole fraction of reactant in the effluent gas stream (use of MS and IR gas analyzers). All pseudo-steady state catalytic activity results obtained on the 5 wt% Ni supported on CeO_2-NR and CeO_2-NP were reproducible within 3–5%.

The amount of carbon (mg C g^{-1} or wt%) accumulated after 12 h of DRM (20% CH_4, $CH_4/CO_2 = 1$) at 700 °C was estimated via temperature-programmed oxidation (TPO) experiments through which kinetic features of the carbon oxidation were also studied. Following DRM reaction at 700 °C, the reactor was purged in He gas flow at 700 °C until the CO_2 and CO signals attained their respective background value. The reactor temperature was then decreased to 100 °C in He gas flow, and the feed was then switched to 10% O_2/He (50 NmL min^{-1}), while at the same time the temperature was increased to 700 °C (TPO, β = 30 °C min^{-1}). During TPO, CO and CO_2 signals were continuously monitored by MS (m/z = 28 and 44, respectively) and converted into concentration by using certified gas mixtures (2% CO/He and 1% CO_2/He). The transient rates of CO and CO_2 production in the TPO run were estimated after using appropriate material balances.

2.4. Quantification of carbon oxidation to CO(g) by lattice oxygen of CeO_2 during DRM

Dry reforming of methane was conducted following exchange of the lattice ^{16}O of CeO_2 support for ^{18}O at 700 °C to a large extent. The aim was to compare (in a quantitative manner) the participation of the lattice oxygen of ceria support ($O\text{-}_L$) to that of oxygen derived from the CO_2 activation route (e.g., $CO_2\text{-}s + s \rightarrow CO\text{-}s + O\text{-}s$; s is a surface Ni site) towards oxidation of carbon to CO(g) [25]. The carbon on Ni/CeO_2 is largely derived by CH_4 decomposition as recently reported by us for different ceria preparation routes [64]. A fresh catalyst sample (W_{cat} = 20 mg diluted with 30-mg SiC) after purged in Ar gas flow at 700 °C was exposed to 2% $^{18}O_2$/1% Kr/He for 10 min. During this gas treatment, the $^{16}O_2$ ($m/z = 32$), $^{16}O^{18}O$ ($m/z = 34$), $^{18}O_2$ ($m/z = 36$) and Kr ($m/z = 84$) were monitored continuously by on-line MS. The amount of oxygen exchanged (mol $^{16}O\ g^{-1}$) was estimated after calibration of the MS signals and using the appropriate material balance. The temperature of the solid was then decreased to 400 °C in the flow of $^{18}O_2$/Ar gas mixture, followed by a 10-min Ar purge. The gas flow was then switched to pure H_2 (1 bar) for 1 h for reducing only the $Ni^{18}O$ to Ni^0; a very small reduction of ^{18}O-containing ceria was recorded at 400 °C [25]. Subsequently, the feed was switched to Ar for 10 min until the H_2 MS signal reached its background value, followed by an increase of the temperature to 655 °C (lowest T investigated). A step-gas switch to the DRM gas mixture (20 vol% CH_4/20 vol% CO_2/1 vol% Kr/He) at 655 °C was then made. During the latter switch, the dynamics of carbon oxidation (carbon was derived mainly via CH_4 activation) by the support ^{18}O-lattice oxygen ($^{18}O\text{-}_L$) and the ^{16}O-derived from the CO_2 activation on the Ni surface ($^{16}O\text{-}_s$) were probed by the formation of $C^{18}O$ and $C^{16}O$ gases, respectively. The same experiment was conducted at higher temperatures (670, 685 and 700 °C) following oxidation of the catalyst sample at 700 °C (20% O_2/He, 1 h).

During the step-gas switch to the DRM gas mixture, the likely

formation of $C^{16}O^{18}O$ and $C^{18}O_2$ due to an exchange of $^{18}O_{-L}$ with $C^{16}O_2$, and the subsequent reforming reaction of CH_4 with $C^{16}O^{18}O$ and $C^{18}O_2$ to form $C^{18}O$(g) was considered. For this, after the $^{16}O/^{18}O$ isotopic exchange, the step-gas switch He → 20% $C^{16}O_2$/1% Kr/He was made, where the $C^{16}O^{18}O$ ($m/z = 46$), $C^{18}O_2$ ($m/z = 48$) and $C^{18}O$ ($m/z = 30$) transient response curves were recorded, and appropriate interpretation was provided [25]. Calibration of the $C^{18}O$ ($m/z = 30$) MS signal to concentration (mol%) was made after using a standard $C^{18}O$/He isotopic gas mixture. Contributions of $C^{18}O_2$ ($m/z = 48$) and $C^{16}O^{18}O$ ($m/z = 46$) to the $m/z = 30$ ($C^{18}O$) signal were measured via the use of standard $C^{18}O_2$/He and $C^{16}O_2$/He gas mixtures. From these values, an average contribution of $C^{16}O^{18}O$ to $m/z = 30$ was estimated.

3. Results and discussion

3.1. Structural and morphological features of bare CeO_2 and Ni/CeO_2 solids

3.1.1. Powder XRD

The powder XRD patterns of CeO_2 and Ni/CeO_2 samples are depicted in Fig. 1. The diffraction peaks at 28.5, 33.1, 47.5 and 56.3° correspond to the (111), (200), (220) and (311) planes, respectively, and are attributed to the face-centered cubic CeO_2 in which each cerium cation is surrounded by eight oxygen anions (JCPDS card: 00–043–1002) [52]. For the as-prepared Ni/CeO_2 samples, diffraction signals matched to indexed CeO_2 cubic structure. The weak diffraction peaks at 37.3° and 43.4° were assigned to the (111) and (200) planes, respectively, of the NiO cubic phase (JCPDS card: 01–075–0197). Table 1 presents the mean crystallite sizes of CeO_2 and NiO estimated by the Scherrer Eq. (3).

3.1.2. High resolution transmission electron microscopy (HR-TEM)

The morphology of CeO_2 and Ni/CeO_2 samples was investigated by transmission electron microscopy (TEM) and high-resolution TEM (HR-TEM) analyses. CeO_2-NR (Fig. 2**a**) exhibits a well-defined *rod–like* morphology. The diameter of CeO_2 nanorods is ca. 10–20 nm, while their length varies in the 50–200 nm range. The same distinct morphology, i.e. nanorods, was obtained after calcination at 500 °C [56,60], demonstrating that the increase of oxygen gas pretreatment temperature to 700 °C does not affect the shape of ceria nanorods. As illustrated in Fig. 2**d**, d-spacings in the crystal lattice of CeO_2-NR were identified to take the values of 0.26 and 0.30 nm, which correspond to the (200) and (111) crystal planes, respectively, in full agreement with the pXRD results (Fig. 1). This in turn indicates that the dominant

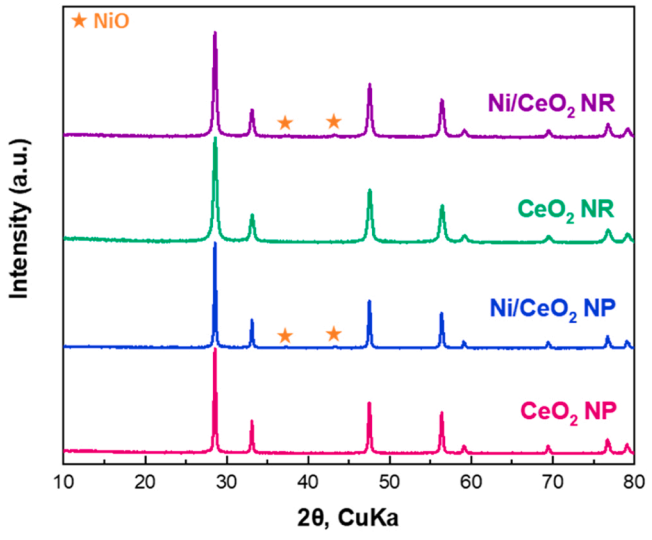

Fig. 1. Powder X-ray diffraction patterns of bare CeO_2 and Ni/CeO_2 samples of different ceria morphology (shape).

Table 1
Structural characteristics of bare CeO_2 and Ni/CeO_2 of different ceria morphologies.

Sample	XRD						TEM
	CeO_2 (111)			NiO (200)			NiO/Ni mean particle size
	d_{XRD} (nm)	d_{111} (nm)	α (nm)	d_{XRD} (nm)	d_{200} (nm)	α (nm)	
CeO_2-NP	33.4	0.312	0.541	-	-	-	-
Ni/CeO_2-NP	35.8	0.312	0.541	25.4	0.209	0.362	24.4 ± 4.0/ 20.7 ±3.4
CeO_2-NR	17.4	0.312	0.540	-	-	-	-
Ni/CeO_2-NR	20.9	0.312	0.541	19.7	0.209	0.362	20.3 ± 4.8/ 17.2 ± 4

surface crystal facets of the rod-shaped CeO_2 sample appear to be the {100} and {110}, in agreement with relevant studies [82,83]. On the other hand, CeO_2-NP (Fig. 2**b**) displays an irregular *polyhedral-like* shape with a mean particle size of ~ 40 nm. It is worth mentioning that calcination at lower temperatures (ca. 500 °C) of the same material resulted in ceria nanoparticles of *cubic-like* instead of *irregular polyhedral-like* morphology [56,60]. This most probably implies the collapse of nanocubes-like structure at T > 500 °C, as opposed to nanorods.

Ceria in Ni/CeO_2-NR retains the rod–like morphology of bare CeO_2 nanorods, indicating no further structural modification upon Ni addition and an additional calcination step (Fig. 2**c**). Isolated NiO particles of spherical shape can be distinguished (Fig. 2c), clearly shown in the representative HR-TEM image (Fig. 2**d**). The size of NiO spherical particles varies from 10 to 30 nm, with a mean particle size of ca. 20 nm (Fig. 2c). These findings are in line with the pXRD results (Table 1). As seen in Fig. 2d, the lattice fringes of NiO and CeO_2 are well defined reflecting the crystallinity of the sample. The observed lattice d-spacing for the NiO and CeO_2 phases is 0.21 and 0.3 nm, respectively, which confirms the presence of NiO particles exposing (200) planes which are in contact with CeO_2 (111) planes, in agreement with the pXRD analysis (Fig. 1).

Ceria in Ni/CeO_2-NP (Fig. 2**e**) exhibits irregular shapes of CeO_2 polyhedron-like, while agglomerated NiO particles (10–30 nm, mean particle size of 24.4 nm) are detected. The HR-TEM results of Ni/CeO_2-NP are displayed in Fig. 2 **f**. The lattice d-spacing of 0.21 nm is ascribed to the NiO (200) crystal plane, revealing the presence of agglomerated NiO particles. It is worth noticing the twice as large mean particle size of CeO_2 in the case of CeO_2-NP sample compared to that in the case of CeO_2-NR (33.4 vs 17.4 nm, Table 1). In contrast, the mean Ni particle size is within 15% for the two samples according to the TEM results (Table 1). These findings will be further corroborated in conjunction to the transient kinetic and reactivity studies (*vide infra*).

3.1.3. In situ Raman spectroscopy

Fig. 3 shows *in situ* Raman spectra obtained at 450 °C for the bare CeO_2-NP and CeO_2-NR supports and the supported Ni metal catalysts after 1 h in 20% O_2/He gas-flow (see Experimental Section 2.2.1). Cerium(IV) oxide crystallizes in the fluorite cubic structure (*Fm3m*), of which the vibrational structure is simple, previewing one single Raman active mode (F_{2g}), typically observed at ~ 465 cm^{-1}, a value which is relevant for perfect ceria lattice at room temperature. The F_{2g} position and width is sensitive to temperature and particle size. A red shift and a width increase are caused by increasing the particle size. Additionally, F_{2g} undergoes a red shift at elevated temperatures due to, inter alia, lattice expansion, depopulation of the ground vibrational state, and anharmonic effects. Due to partial relaxation of symmetry rules caused by lattice defects, additional bands can typically be discerned, *ca.* at 250 cm^{-1} (attributed to ideally Raman-inactive transverse acoustic mode) and 590 cm^{-1} (defect-induced mode, "D" band) [73,84].

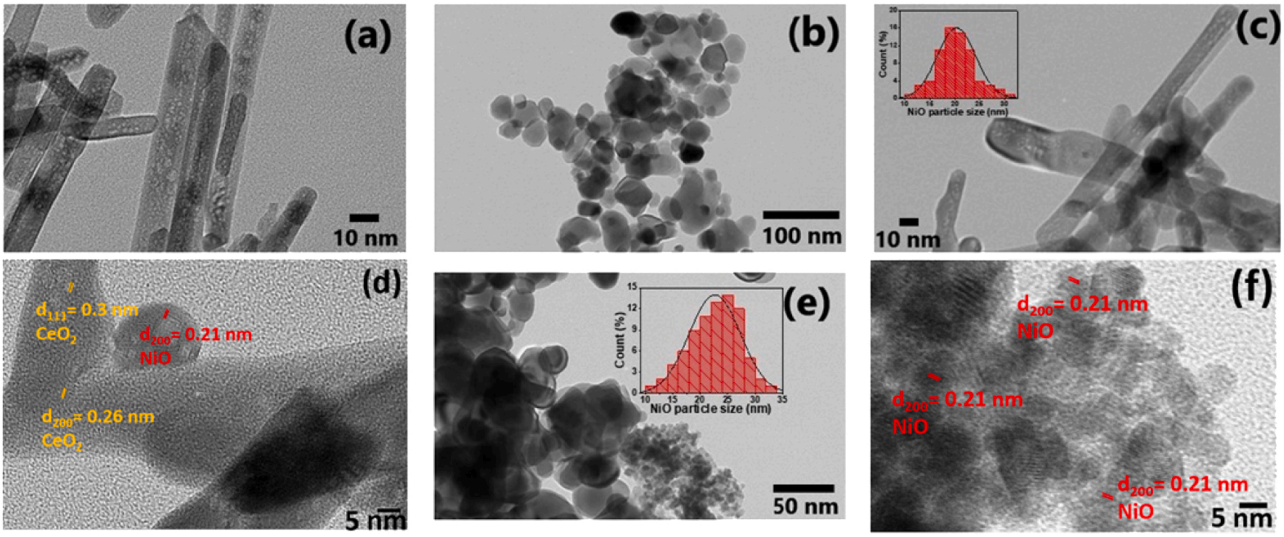

Fig. 2. (a, c) TEM image of CeO_2-NR, (b, e) TEM image of CeO_2-NP, (d) HR-TEM image of Ni/CeO_2-NR, and (f) HR-TEM image of Ni/CeO_2-NP.

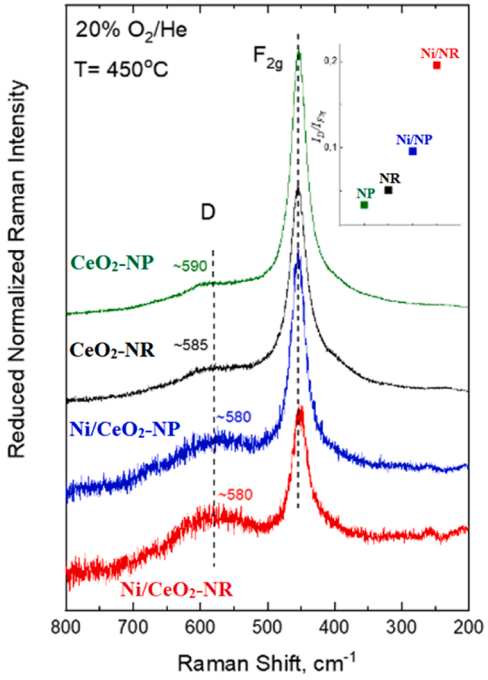

Fig. 3. *In situ* Raman spectra obtained at 450 °C under flowing (30 NmL min^{-1}) 20% O_2/He gas mixture over the bare CeO_2-NR and CeO_2-NP supports and the associated supported Ni catalysts. Inset: intensity ratio $I_D/I_{F_{2g}}$(see text). Recording conditions: laser wavelength, λ_0 = 491.5 *nm*; laser power, 15 mW; spectral slit width, 7 cm^{-1}; time constant, 1.2 s.

Lattice deformations result in defect generation and creation of oxygen vacancies by oxygen atom relocations from the interior of cation sublattices tetrahedral sites to the ideally vacant cationic octahedral sublattice sites (interstitial sites) [85]. The extent of such defects and vacancies is reflected by the $I_D/I_{F_{2g}}$ratio [73], which is plotted in the inset of Fig. 3. The topology of defects and vacancies is of direct relevance to the oxygen mobility and diffusivity in the bulk of ceria, which are of key importance to the functionality of the material (oxygen storage and release). Likewise, the defect topology greatly affects and determines the Raman fingerprint (obtained under well-controlled conditions) of the anionic sublattice in each case [73,74]. Hence, comparisons of Raman fingerprints pertaining to ceria materials exhibiting seemingly identical structures (*i.e.*, based on XRD analysis), reveal differences in the relative concentration of defects among the studied materials. Fig. 3 shows a higher relative richness/concentration of defects/vacancies/interstitials for CeO_2-NR compared to CeO_2-NP. Incorporation of Ni to bare ceria promotes the creation of defects, while maintaining a much higher extent for the NR morphology, evidenced by the nearly double $I_D/I_{F_{2g}}$ value obtained compared to the CeO_2-NP counterpart material (inset Fig. 3). Qin et al. [86] performed UV–vis/Raman studies on a series of Ni supported on CeO_2 nanorods, nanoparticles and nanocubes, and reported that the density of oxygen vacancies followed the order: CeO_2-R > CeO_2-P > CeO_2-C. UV–vis/Raman spectroscopy and PALS techniques used by Huang and Gao [87] showed by the observed $I_D/I_{F_{2g}}$ values for CeO_2 nanorods and nanocubes that the concentration of oxygen vacant sites in the CeO_2-NR carrier is larger, and that the average oxygen vacant sites cluster size is smaller having lower average electron density, in comparison to the CeO_2 cubes. Defects, such as oxygen vacancies, are considered crucial for catalytic reactions, especially on CeO_2 surfaces, as they can stabilize transition metal nanoparticles. Additionally, lattice oxygen can be supplied for the oxidation of an active species, leaving an oxygen vacant site behind, which can bind adsorbates more strongly, thus assisting their dissociation [88,89]. This important issue is elaborated in Sections 3.2 and 3.4.

We have previously shown that the "D" band is a convolution of at least two components [73,90]: (a) band "D1" located above 600 cm^{-1}, and which is assigned to Ce-O modes, involves labile/detachable O atoms (e.g., at interstitial sites) that can be reduced/transported under H_2 reducing conditions, and (b) band "D2" located below 600 cm^{-1}, and which is assigned to modes within coordinatively unsaturated sites, such as MO_7 that remain unaffected under reducing conditions. Hence, the previously described approach of sequential *in situ* Raman spectra recorded under oxidizing (20% O_2/He) and reducing (5% H_2/He) conditions was applied for the studied materials [73]. The corresponding difference spectra obtained by subtracting the normalized spectrum obtained under reducing conditions from the counterpart spectrum obtained under oxidizing conditions are shown in Fig. 4. The insets show the "O_2 – H_2" spectra (at the same normalized scale) that provide a steady state measure of the attenuation of band D1, thereby corresponding in each case to the oxygen that was reduced/transported under the applied H_2 reducing conditions. Notably, the difference bands are in the ~ 605–610 cm^{-1} region, thereby confirming that band "D" loses intensity from its high frequency side (*i.e.,* component "D1" is attenuated). Importantly, the "O_2 – H_2" difference band intensity follows the order: Ni/CeO_2-NR > Ni/CeO_2-NP >> CeO_2-NR > CeO_2-NP, thereby

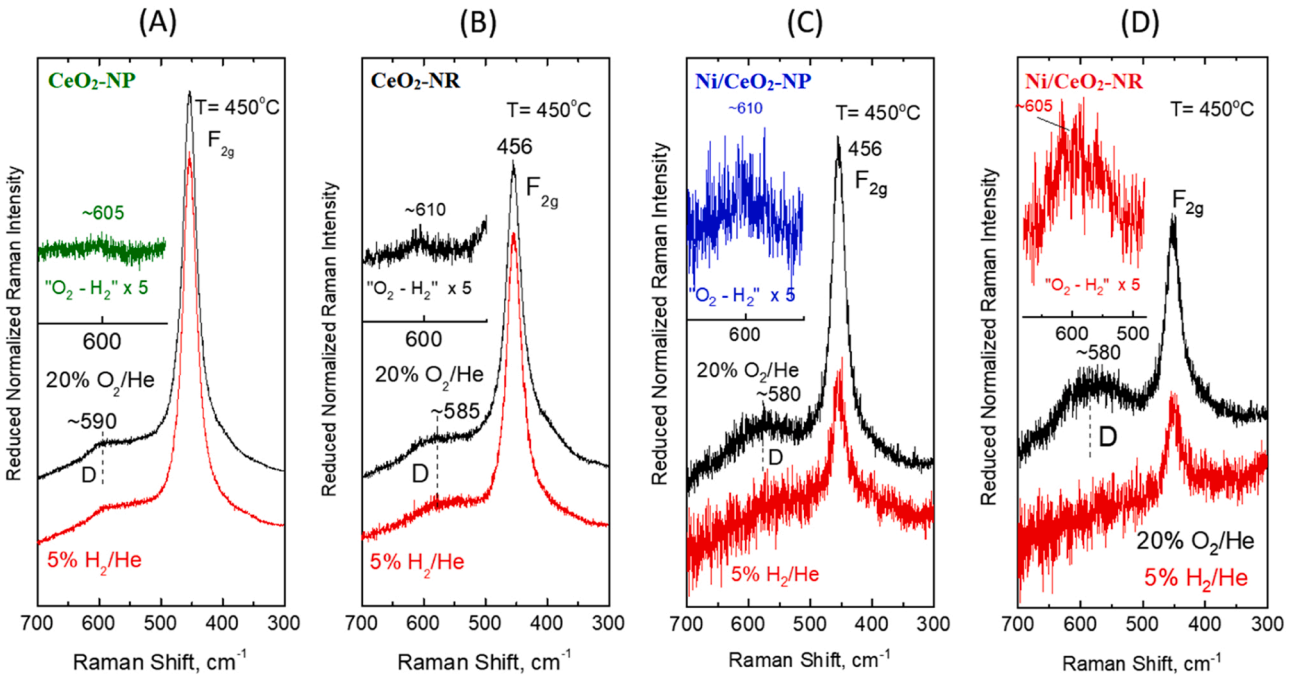

Fig. 4. *In situ* sequential Raman spectra obtained at 450 °C under flowing 20% O_2/He and 5% H_2/He gases as indicated by each spectrum for (A) CeO_2-NP; (B) CeO_2-NR; (C) Ni/CeO_2-NP; (D) Ni/CeO_2-NR. Inset traces are the outcome of subtraction of the spectrum obtained under H_2 gas from the counterpart spectrum obtained under O_2 gas in each case. Recording parameters are given in Fig. 3 caption.

corroborating the corresponding trends in reducibility and oxygen exchange kinetics to be presented and discussed later. Upon recording the in-situ Raman spectra under reducing conditions, the full spectral features observed under oxidizing conditions were reinstated after exposing each sample to the 20% O_2/He gas flow for 30 min.

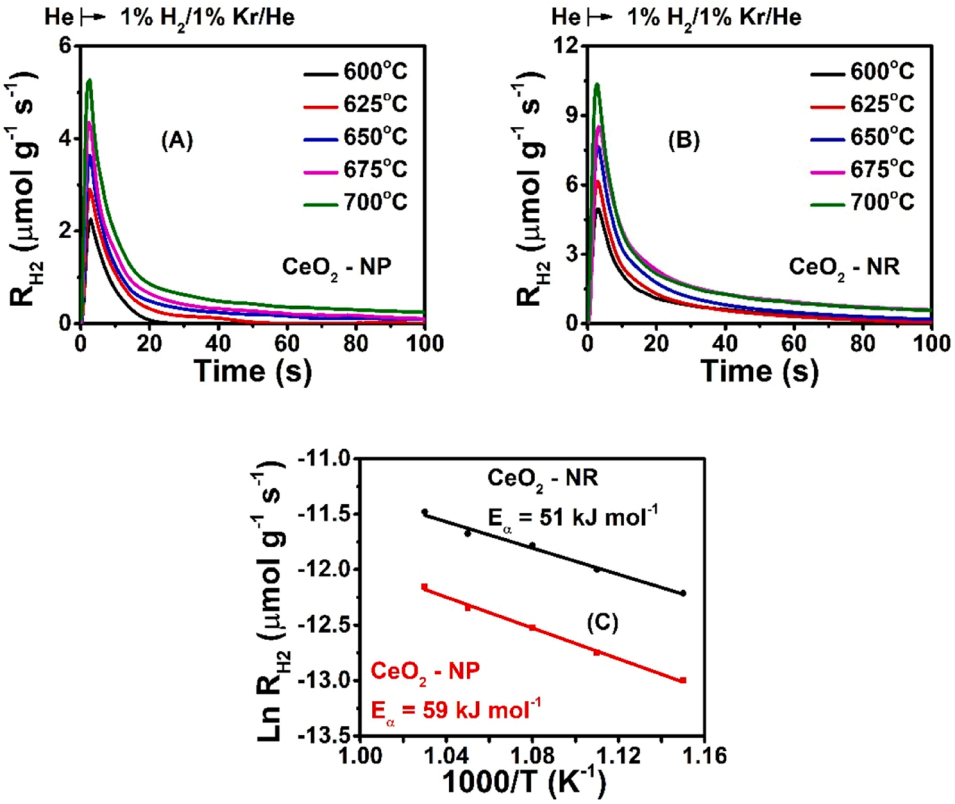

Fig. 5. Dynamic rates of (A) CeO_2-NP and (B) CeO_2-NR solids reduction by hydrogen (μmol g^{-1} s^{-1}) in the 600–700 °C range obtained during H_2-TIR. (C) Determination of the kinetic apparent activation energy (E_α, kJ mol^{-1}) of the surface reduction process of solids. Experimental procedure: 20% O_2/He (700 °C, 2 h) → He (T, 10 min) → 1% H_2/Kr/He (T, t).

3.2. Transient isothermal reduction by hydrogen (H_2-TIR)

Fig. 5**A, B** presents dynamic reduction rates (per gram basis) obtained during H_2-TIR in the 600–700 °C range over the two bare CeO_2-NP and CeO_2-NR supports, respectively. The initial reduction rate in the two solids reflects the reduction of surface lattice oxygen. As reduction time increases, the reduction process is governed by oxygen diffusion in the bulk of the ceria crystal structure (rate-determining step), before oxygen reaches the surface and reacts with hydrogen gas. Thus, the rate of reduction after ca. 10 s increases considerably with increasing reduction temperature (600–700 °C). The tailing part appeared in the transient rate response curves (Fig. 5A, B) should therefore be linked to the slow rate of subsurface lattice oxygen diffusion towards the surface. The reduction rates (per gram basis) are noticeably higher in the case of CeO_2-NR (Fig. 5B) compared to CeO_2-NP (Fig. 5A). The fact that CeO_2-NR has a BET area of ~ 26 $m^2\ g^{-1}$ compared to CeO_2-NP (~ 12 $m^2\ g^{-1}$) after calcination at 700 °C, this results in specific transient reduction rates per unit surface area, R_{H2} (μmol $m^{-2}\ s^{-1}$) slightly larger in the case of CeO_2-NR.

The amount of labile oxygen (μmol O g^{-1}) reduced by hydrogen gas in the two ceria support materials was obtained after integrating the respective transient reduction rate (per gram basis), and results are reported in Table S1. At 600 °C, CeO_2-NR exhibits a significantly larger DOSC when compared to the CeO_2-NP (89.3 vs 18.4 μmol O g^{-1}). After increasing the temperature to 700 °C, the DOSC of CeO_2-NR increases significantly, ca. 3.3 times compared to that at 600 °C, while that of CeO_2-NP increases by 5.1 times. In general, the amount of labile oxygen of CeO_2-NR is significantly larger compared to CeO_2-NP in the 600–700 °C range. These results are consistent with the lower apparent activation energy of surface lattice oxygen reduction estimated for CeO_2-NR ($E_\alpha = 51 \pm 3$ kJ mol^{-1}) and CeO_2-NP ($E_\alpha = 59 \pm 2$ kJ mol^{-1}) as indicated in Fig. 5**C**, and with the larger mobility of subsurface lattice oxygen in CeO_2-NR compared with CeO_2-NP to be demonstrated in the following section. It should be noted that the H_2-TIR results probe for only a small degree (less than 2.6%) of reduction of ceria (few oxygen monolayers), in full agreement with previous works on ceria and doped-ceria materials [34,91].

Li et al. [92] examined the dependence of oxygen storage capacity and lattice O_L diffusion from the bulk to the surface in the case of CeO_2 nano-catalysts on their *shape morphology* (experimental and theoretical studies). An enhancement was found in the case of CeO_2 particles of *nanorod shape*, and which exposed the most stable {100} and {110} facets. Also, Ma et al. [93] and Lorber et al. [68] concluded that CeO_2 nanorods had higher degree of reduction compared to CeO_2 nanocubes after conducting H_2-TPR studies on CeO_2-supported Ru and Ni of different ceria morphologies. In addition, the higher reducibility of Ni supported on CeO_2 nanorods, terminated predominantly with the {111} facet, promoted carbon oxidation by the participation of mobile oxygen species originating from the CO_2 activation route (DRM reaction conditions) [68,94]. The present results (Fig. 5 and Table S1) suggest a weaker bonding between Ce^{3+}/Ce^{4+} and O^{2-} of the CeO_2-NR, in agreement with the Raman findings (*vice supra*) and the transient isotopic results to be presented and discussed later.

3.3. Probing the lattice oxygen mobility of CeO_2 supports of different morphology

The mobility of lattice oxygen (surface/bulk) of metal oxides used as supports of catalytic phase(s) and their ability to possess oxygen vacant sites has been shown to be an important parameter for many catalytic reactions [74,75,95,96]. The TIIE technique ($^{16}O/^{18}O$ exchange) was proven sensitive to study differences in the dynamics of lattice oxygen (O_L) mobility (diffusion) and oxygen sublattice structure for the present CeO_2 supports of different morphology (shape) [75]. Fig. 6**A** displays the dynamic evolution of the total rate of $^{16}O/^{18}O$ exchange (R_{16O}, μmol $g^{-1}\ s^{-1}$) at 660 °C for the CeO_2-NR and CeO_2-NP solids. Significantly larger initial rates of surface and bulk oxygen exchange of $^{16}O/^{18}O$ were observed for the CeO_2-NR compared to CeO_2-NP. These variations are due to differences in the intrinsic kinetic rate of surface $^{16}O/^{18}O$ exchange (Ce-O-Ce and Ce-V_o-Ce bonding) and subsurface $^{16}O_L$ diffusion towards the surface, as the result of the *different morphology* of the CeO_2-NR and CeO_2-NP solids [75]. Fig. 6**B** presents the variation of the descriptor parameter $\alpha_g^{(18)}$ with time during the $^{16}O/^{18}O$ exchange processes (TIIE) conducted at 660 °C over the CeO_2-NR and CeO_2-NP solids. This $\alpha_g^{(18)}$ descriptor parameter is very informative about the dynamics of oxygen diffusion and exchange at the beginning of the process (surface $^{16}O/^{18}O$ exchange) and during the whole TIIE dynamic process [75,97]. In particular, the steepness of the $\alpha_g^{(18)}(t)$ at the initial period of the transient is connected to the small value of D_{eff} for oxygen diffusion in the bulk of ceria, whereas small values of $\alpha_g^{(18)}(t)$ indicate large rates of $^{16}O/^{18}O$ exchange (large consumption of $^{18}O_2(g)$, thus the numerator in Eq. (11) takes small values) [75,97].

As shown in Fig. 6B, the $\alpha_g^{(18)}$ of CeO_2-NP is steeper at the initial stage (higher energy barrier for $^{16}O/^{18}O$ surface exchange) [98], and it is also higher compared to the CeO_2-NR, practically in most of the transient $^{16}O/^{18}O$ exchange (ca. up to 400 s). This illustrates that the exchange rate of $^{16}O_L$ for $^{18}O_S$ (surface oxygen), which passes through diffusion of sub-lattice $^{16}O_L$ towards the surface, is slower in the CeO_2-NP solid; a larger fraction of ^{18}O is found in the gas-phase (Eq. (11)). Another important feature derived from the analysis of the $\alpha_g^{(18)}(t)$ parameter is the time at which 50 at% of ^{18}O is in the gas-phase during TIIE, named $t_{0.5,\ \alpha_g^{(18)}}$ (s). The latter parameter for the CeO_2-NR was estimated at ~ 17.5 s to be compared with ~ 5.9 s for the CeO_2-NP. Therefore, in harmony with the previously reported results obtained by Raman

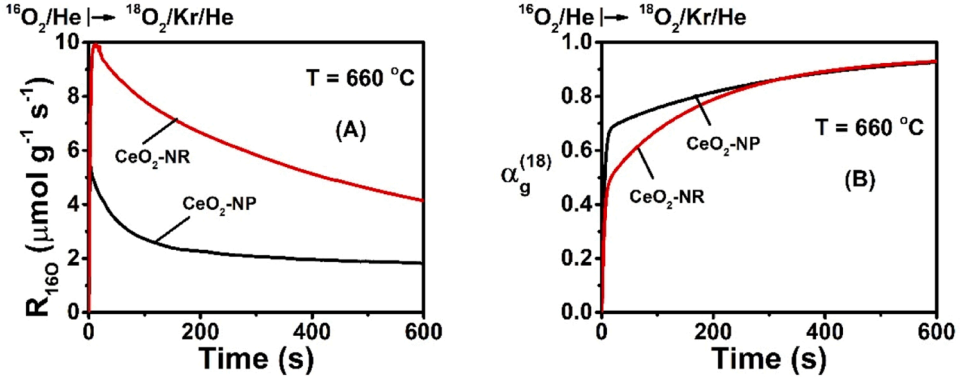

Fig. 6. (A) Dynamic rates of the total $^{16}O/^{18}O$ exchange process (μmol $g^{-1}\ s^{-1}$). (B) $\alpha_g^{(18)}$ descriptor parameter as a function of time obtained during the $^{18}O_2$-TIIE at 660 °C conducted on the CeO_2-NR and CeO_2-NP solids. Experimental procedure: 20% O_2/He (700 °C, 2 h) → He (10 min) → 2% $^{16}O_2$/He (T, 30 min) → 2% $^{18}O_2$/Kr/He (T, t).

(Fig. 3) and H_2-TIR (Fig. 5C), the CeO_2-NP exhibits less amount (per gram basis) of labile surface and bulk lattice oxygen available for $^{16}O/^{18}O$ exchange.

The TIIE technique allowed also to use the $^{16}O^{18}O$ transient response curves obtained at different temperatures to estimate an apparent activation energy for the bulk oxygen diffusion, according to Eq. (12). Figures S1A and S2A show that the dynamic rates of $^{16}O^{18}O$ formation obtained on CeO_2-NR and CeO_2-NP, respectively, present largely different features (broadness of the shape at the initial stage of the transient, and magnitude of rates). More precisely, the $R^{16}O^{18}O$ transient curve obtained at 660 °C on CeO_2-NP presents a sharp peak of ~ 1.5 μmol g^{-1} s^{-1} (surface $^{16}O/^{18}O$ exchange) at ~ 50 s, followed by a long tail of ~ 1 μmol g^{-1} s^{-1} (bulk oxygen diffusion) up to 1200 s of the experiment. On the other hand, the CeO_2-NR (Fig. S1A) presents a single broad peak with a maximum value of ~ 2 μmol g^{-1} s^{-1} at ~ 300 s, followed by a slowly declining rate up to 1200 s. The lower values of dynamic rates obtained on CeO_2-NP are mainly due to the slower subsurface/bulk oxygen diffusion processes because of the lower concentration of oxygen defects according to the Raman results (Figs. 3 and 4), when compared to the CeO_2-NR solid. The oxygen defects concentration influences the activation energy of bulk lattice oxygen diffusion, to be presented and discussed next. At this point it should be mentioned that the crystallite size of ceria also influences the dynamics of bulk oxygen diffusion towards the surface but to a much lesser extent than the energetics of the diffusion process in the bulk of the solid.

The dynamic rates of $^{16}O_2$ formation ($R^{16}O_2$) start immediately upon the switch to the $^{18}O_2$/Kr/He isotopic gas mixture, where a maximum in the rate is reached at very short times with significant drop after the first ~ 300 s (Figures S1B and S2B), as opposed to those of $R^{16}O^{18}O$ (Figs S1A and S2A). This feature is determined by the relative mechanism and kinetics of $^{16}O/^{18}O$ exchange leading to $^{16}O_2$(g) [99].

Table S2 provides the amounts (μmol g^{-1}) of $^{16}O^{18}O$ and $^{16}O_2$ and that of total ^{16}O exchanged after 20 min of $^{16}O/^{18}O$ exchange at different temperatures. It is illustrated again that the CeO_2-NR sample has a significantly larger ability to deliver lattice oxygen to the surface than the CeO_2-NP at the same temperature. For example, at 660 °C, CeO_2-NR had the ability to exchange ~ 3.2 times a larger amount of ^{16}O for ^{18}O than CeO_2-NP (Table S2, last column). The amount of exchangeable oxygen reported in Table S2 is in line with those reported for various doped ceria materials produced industrially [75].

Fig. 7 presents the obtained results after linearization of Eq. (12) and considering an Arrhenius relationship for D_b. It is clearly shown that CeO_2-NR exhibits a significantly lower apparent activation energy for bulk oxygen diffusion (E_b = 245 ± 9 kJ mol^{-1}) compared to the CeO_2-NP (E_b = 334±16 kJ mol^{-1}). These values are in line with those reported for other ceria-based materials [100–102]. The importance of oxygen mobility within the bulk of ceria crystal structure in catalytic reactions was also addressed by Liu et al. [103] in the case of CO

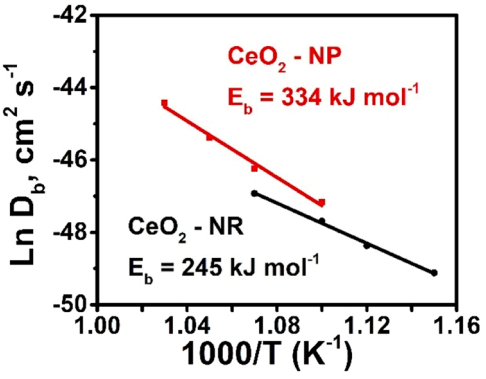

Fig. 7. Determination of the apparent activation energy (E_b, kJ mol^{-1}) for bulk lattice oxygen diffusion in CeO_2-NR and CeO_2-NP solids.

oxidation over CeO_2 nanorods with larger and smaller in size clusters of oxygen vacant sites (defect). It was shown that the former exhibit better catalytic activity due to the faster activation and diffusion of oxygen anions, thus enhancing oxygen supply to the surface.

3.4. CO_2 activation on oxygen vacancies of CeO_2-NR and CeO_2-NP solids

The elementary step of CO_2 dissociation on the oxygen vacancies of reducible metal oxides towards the formation of CO (CO_2(g) + V_O → CO (g) + O_L) becomes an important alternative step of CO_2 activation for the DRM reaction over reducible metal oxides-supported Ni catalysts. The dynamic rates (μmol g^{-1} s^{-1}) of CO_2 consumption and CO formation obtained during the step-gas switch He → 1 vol% CO_2/1 vol% Kr/He(t) at 700 °C over the two bare CeO_2 supports, which were first pretreated in H_2/He gas stream (700 °C/30 min, Section 2.2.4), are depicted in Figs. 8**A** and 8**B**, respectively. It is seen that CO_2 chemisorption starts immediately after the switch to the CO_2 gas mixture for both solids. However, the rate profiles in terms of shape and time at which maximum rate appears (t_{max}) are different. The amount of CO formed during the first 60 s of the transient (no further CO formation was noticed, Fig. 8A-B) was found to be ~ 3.35 times larger for CeO_2-NR compared to CeO_2-NP (Table S3).

The specific rate of CO_2 consumption per unit surface area of ceria (μmol m^{-2} s^{-1}) could be expressed as $R_{CO2} = k\ P_{CO2}\ C_{VO}$, where C_{VO} is the surface concentration of oxygen vacant sites. An attempt to compare the ratio of the kinetic rate constants associated with the CO_2 dissociation step on the oxygen vacant sites for the two ceria samples, the transient rates shown in Figs. 8A and 8B at $t = t_{max}$ (time at maximum rate), and the H_2-TIR results at 700 °C (Table S1; 1 μmol H_2/g is equivalent to 1 μmol O_L/g) were used. The latter information was used to estimate the ratio of the concentration of surface oxygen vacancies formed after hydrogen reduction in the two solids, assuming to be similar to that obtained after H_2-TIR at 700 °C (Table S1). The P_{CO2} at t_{max} was estimated using the CO_2 concentration recorded at t_{max} for each solid. It was found that k^{NR}/k^{NP} equals ~ 1.3, suggesting that the surface of CeO_2-NR appears more active towards CO_2 dissociation on the surface oxygen vacant sites.

Huang and Gao [87] in their review paper noted that CeO_2 nanoparticles surface chemistry and morphology could amend the amount and structure of oxygen vacant sites, while oxygen basicity character could enhance CO_2 adsorption and dissociation in the presence of V_O. The adsorbed oxygen formed facilitates reduction of coking via combustion to CO(g) during the DRM reaction [104,105]. The extent of participation of lattice oxygen towards carbon gasification is presented and discussed in the following Section 3.6.

In line with the above observations, Mai et al. [106] suggested that a shape-targeted synthesis methodology of CeO_2 nanoparticles could impart supports with high oxygen storage capacity. In fact, they reported that CeO_2 nanorods (enhanced population of (110) and (100) facets) led to larger amounts (per gram basis) of oxygen vacant sites, which decreases in the case of CeO_2 nanocubes and nanopolyhedra, in good agreement with the present findings. This was explained as due to diffusional restrictions imposed on the surface and bulk oxygens, as the surface structure exposing (111) facets exhibits a lower diffusivity value for O_L migration towards the surface when compared to the ceria surface exposing more the (100) and (110) facets. In addition, He et al. [107] reported that 3 wt% Ru-based catalysts supported on CeO_2-NR (nanorods) and CeO_2-NC (nanocubes) mainly exposed (110) and (100) facets with a higher oxygen vacancy concentration compared to the case of CeO_2-NP, which exposed the (111) facets. It was concluded that the former two catalytic systems with better performance had higher surface energy, which enhances the interaction between Ru and CeO_2.

The amount of CO formed is only slightly lower than that of CO_2 consumed for both solids (Fig. 8A, B), suggesting that a small only amount of CO_2 was irreversibly adsorbed on the CeO_2 surface at 700 °C [108], confirming also the elementary reaction step: CO_2(g) + V_0 → CO

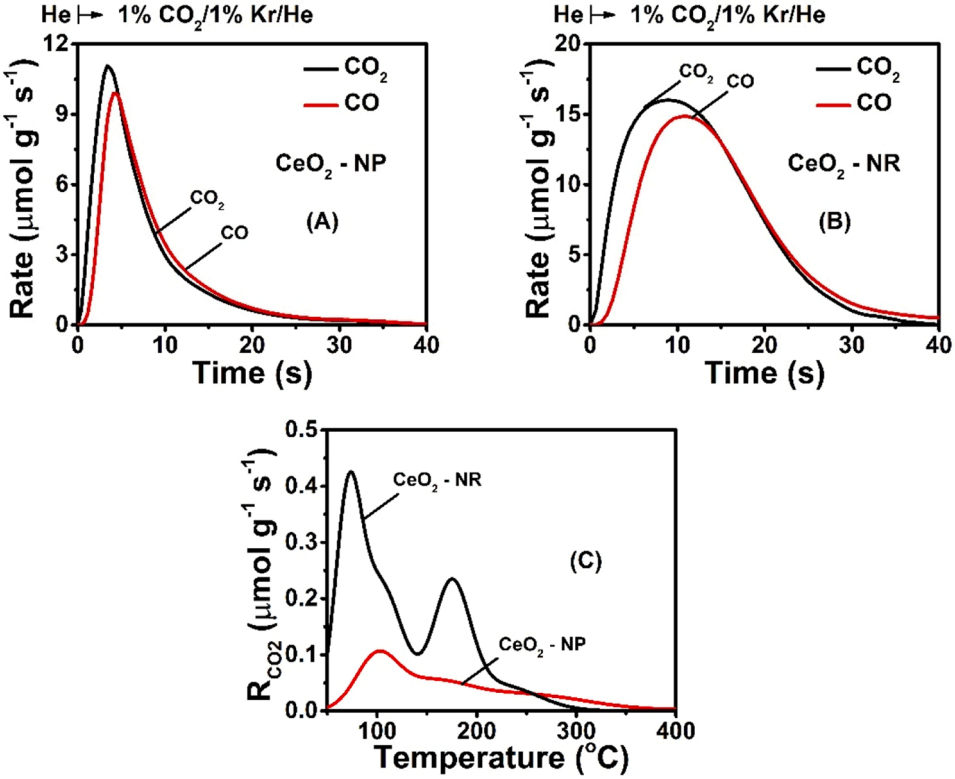

Fig. 8. Transient rates (μmol $g^{-1}s^{-1}$) of CO_2 consumption and CO formation over CeO_2-NP (A) and CeO_2-NR (B) after the step-gas switch He → 1% CO_2/1% Kr/He (t) at 700 °C. (C) CO_2-TPD rate profiles for the CeO_2-NP and CeO_2-NR bare supports. Experimental procedure: 20% O_2/He (700 °C, 2 h) → He (10 min) → 2% H_2/He (700 °C, 30 min) → He (10 min) → 1% CO_2/Kr/He (700 °C, t) → He (10 min), cool down to 30 °C → 1% CO_2/He (30 °C, 30 min) → TPD (β = 30 °C min^{-1}).

(g) + O_{-L}. These results are in good agreement with XPS and DFT studies [11,109–111], where oxygen vacant sites of CeO_2 carriers are offered for CO_2 dissociation.

Fig. 8**C** presents the CO_2 rate profiles (μmol g^{-1} s^{-1}) obtained during temperature programmed desorption (TPD) of pre-adsorbed CO_2 at 30 °C over the bare CeO_2-NP and CeO_2-NR carriers. The latter solid exhibits two well-resolved desorption peaks centred at ~ 70 °C and 180 °C with shoulders on the high-T side (~ 100 °C and 220 °C) of the response curve. These are attributed to the presence of weak and moderate basic sites, respectively [112]. On the other hand, the CO_2 desorption profile of CeO_2-NP shows a single desorption peak at ~ 100 °C with a broad shoulder (ending at ~ 400 °C), suggesting the existence of a distribution of basic sites of higher strength. Table S4 reports the surface concentration (μmol g^{-1} and μmol m^{-2}) and peak centre (T_M, °C) corresponding to the various basic sites of each of the CeO_2 carrier morphology after performing deconvolution (gaussian peak shape) of the CO_2-TPD traces. The total surface concentration of basic sites expressed in μmol g^{-1} and μmol m^{-2} is higher by a factor of ~ 2.7 and 1.2, respectively, in the case of CeO_2-NR when compared to CeO_2-NP. On the other hand, the distribution among the weak (peaks 1 and 2) and stronger sites (peaks 3 and 4) appears similar (ca. 60 vs 40%) for the two solids. Considering that the dominant crystal facets of CeO_2-NR are (100) and (110), whereas CeO_2-NP comprises of irregular-shaped nanoparticles with no distinct planes, a relationship between surface morphology and basicity could be considered. In a similar manner, Chen et al. [112] studied the influence of CeO_2 morphology on the basicity of four different solids after applying the CO_2-TPD technique. The spindle-like CeO_2 presented the highest basicity followed by the rod-like [112], precipitated, and cubic CeO_2. CO_2-TPD and CH_4-TPD traces obtained on a series of CeO_2-supported Pt catalysts with different support morphologies revealed that CO_2 adsorption is stronger on Pt/CeO_2-R due to its largest content of exposed Ce^{3+} and V_O sites, while CH_4 chemisorption was affected by the exposed surface Pt atoms [113]. In agreement with previous observations [114], Ni supported on bare CeO_2 and ceria doped with 3 wt% Ga resulted in an increased concentration of basic sites of medium strength and Ni dispersion. However, further increase of Ga (5 wt%) led to an increase of the strong basic sites, thus weakening CO_2 activation. Wu et al. [115] explored by means of IR spectroscopy the surface structure effect on acid-base properties of ceria nanocrystals of different morphologies, ca. cubes, octahedra and rods with well-defined crystal facets. It was found that weak Lewis acid sites of similar strength were present in all ceria nanoshapes, whereas two types of basic sites, i.e. hydroxyl groups and surface lattice oxygen, were identified with their amount and strength being shape-dependent, following the order: rods > cubes > octahedra. Tan et al. [116] were able to distinguish surface Ce species of different Lewis acidity by ^{31}P magic angle spinning NMR studies. This was facet-dependent with Ce^{4+}-like on the (111) facet, and Ce^{3+}-like on the (100) facet.

As will be shown and discussed next, Ni supported on CeO_2-NR presents significantly lower amounts of accumulated carbon after 12 h of DRM at 700 °C, and higher kinetic rates compared to Ni/CeO_2-NP, supporting the view that basic sites are important towards reduction in the rate of inactive carbon accumulation, which is in agreement with previous studies [117–119]. Ma et al. [93] also reported that the increased basicity and the exposed facets of CeO_2 nanorods carrier of Ru enhanced the activity of ammonia synthesis when compared to the nanocubes and irregular-shaped nanoparticles. The latter was correlated with the enhancement of electron donation from ceria to the Ru metal under reaction conditions.

3.5. Kinetic rates and carbon accumulation on Ni/CeO_2-NR and Ni/CeO_2-NP

Kinetic rates of the DRM reaction (20% CH_4/20% CO_2/He) in terms of TOF_{CH4} (s^{-1}) in the 655–700 °C range for the 5 wt% Ni/CeO_2-NR and 5 wt% Ni/CeO_2-NP catalysts are presented in Fig. 9 (Arrhenius plot).

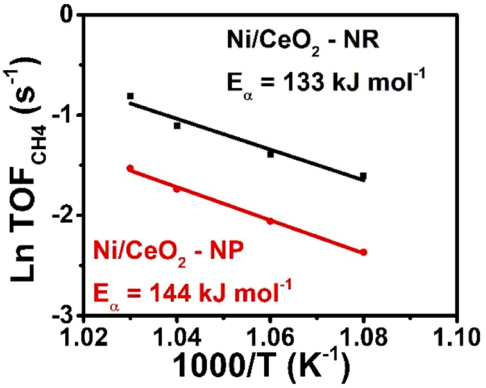

Fig. 9. TOF_{CH4} (s^{-1}) kinetic rates of the DRM in the 655–700 °C range obtained over the Ni/CeO_2-NP and Ni/CeO_2-NR catalysts (20%CH_4; CH_4/CO_2=1; 30 min time-on-stream).

The CH_4 reactant conversion at all temperatures was kept below 15%. An apparent activation energy of 133 ± 6 and 144 ± 4 kJ mol^{-1} was estimated for the Ni/CeO_2-NR and Ni/CeO_2-NP catalysts, respectively. It should be noted here that reported TOF (s^{-1}) values assume that all exposed Ni surface sites participate in the catalytic cycle of DRM. Ideally, the measured TOF should had been expressed as Σ (f_i x TOF_i), where f_i is the fraction of total active sites (N_T) having a site activity TOF_i (s^{-1}). The N_T parameter is very difficult to determine experimentally under working DRM reaction conditions, where the best approach for this remains the application of the SSITKA technique [63]. Assuming that the concentration of active sites can be accurately determined under DRM conditions, the f_i parameter related to the active sites present at the Ni-ceria interface or close to that (on the ceria support) is even more difficult to be estimated experimentally.

It is seen that Ni nanoparticles supported on CeO_2-NR exhibit higher kinetic rates and a lower apparent activation energy for the DRM reaction. The fact that the H_2/CO gas ratio was below unity in all temperatures (ca. 0.43–0.53, Table S5), and the CO_2 conversion rate higher than that of CH_4 (Table S5), supports the presence of the RWGS reaction at the examined conditions, in agreement with our previous works on ceria-based supported Ni catalysts [66,120–122]. Considering that the reverse reaction of DRM at CH_4-conversions lower than 15% is rather small compared to the forward one, then the estimated E_{app} (Fig. 9) reflects the energetics of the forward DRM reaction.

In a recent study of DRM over Ni supported on various morphologies of ceria carriers, Ni/CeO_2-NR showed the highest TOF values for reaction temperatures higher than 600 °C compared to the other catalytic systems examined [123]. A plausible reason was recently provided by Raman and XPS studies [113], that the surface of CeO_2 nanorods is more defective as opposed to that exposed by nanocubes and irregular-shaped nanoparticles. This in turn (i) facilitates the anchoring and interaction of Ni with CeO_2, (ii) creates ensembles of active sites of lattice oxygen/-vacant sites for CH_4/CO_2 dissociation, and (iii) promotes the oxidation of adsorbed carbon species leading to an enhanced activity (less concentration of blocked sites by carbon). Additionally, as reported by Lorber et al. [68], the better catalytic activity of Ni/CeO_2 nanorods could be assigned to a synergistic effect between highly dispersed Ni capable to activate CH_4, and the stabilization of reactive mono- and bidentate-carbonates of intermediate binding strength at the nickel-ceria support interface. This in turn promotes CO formation after carbon oxidation by surface lattice oxygen compared to the nanocubes counterparts that show poor redox activity, thus leading to carbon accumulation. These arguments are further corroborated in the present work by the close anchoring and interaction between Ni and CeO_2-NR as opposed to CeO_2-NP according to the HR-TEM images (Fig. 2); isolated Ni nanoparticles submerged on ceria-NR were distinguished as opposed to CeO_2-NP, where Ni agglomerates were detected.

Lorber and his co-workers [68] synthesized a series of CeO_2 solids with different morphologies used to deposit 2 wt% Ni. The catalytic DRM activity in terms of CH_4 and CO_2 integral rates for low temperatures was found to follow the order: nanorods > nanocubes > nanospheres. It was concluded that activation of CH_4 and CO_2 is fast and kinetically balanced, allowing carbon removal under DRM reaction conditions, as opposed to the case of CeO_2 nanocubes – supported Ni, which accumulated an order of magnitude more carbon [20,124]. The latter was mainly correlated with the deficient oxygen supply from the CeO_2 nanocubes to the Ni phase, and the population of more stable inactive polydentate carbonate species on the surface of ceria nanocubes under reaction conditions (DRIFTS studies), thus decreasing oxygen mobility and carbon removal rates [68].

Regarding H_2 and CO reaction products, higher kinetic rates were obtained for Ni supported on CeO_2-NR for the temperature range examined. Both R_{H2} and R_{CO} increased from 24.5 to 57.4 μmol g^{-1} s^{-1}, and from 51.4 to 108.5 μmol g^{-1} s^{-1}, respectively, with increasing reaction temperature (655 to 700 °C). This led to a slight increase of H_2/CO ratio from 0.48 to 0.53. On the other hand, in the case of Ni/CeO_2-NP, despite the increase of R_{H2} and R_{CO} with increasing reaction temperature, the H_2/CO ratio was found to slightly decrease from 0.46 to 0.44. In a recent low-temperature DRM study over Pt/CeO_2 catalysts of different CeO_2 morphologies [113], Pt/CeO_2-NR minimised the effect of RWSG reaction, resulting to higher H_2/CO gas ratio values compared to Pt supported on CeO_2 nanocubes and irregular-shaped nanoparticles.

In the present work, the use of Ni/CeO_2-NR increased the H_2/CO gas ratio (under the kinetic regime) from 0.44 to 0.53 at 700 °C compared to Ni/CeO_2-NP (Table S5). The amount of carbon accumulated after 12 h of DRM at 700 °C (X_{CH4} ~ 15%) over Ni/CeO_2-NR was 4.1 mg C g^{-1} (0.41 wt%) compared to 5.8 mg C g^{-1} (0.58 wt%) obtained on the Ni/CeO_2-NP catalyst. Thus, the use of CeO_2-NR as carrier to deposit 5 wt% Ni provided a significant reduction (ca. 30%) in the rate of carbon accumulation compared to Ni/CeO_2-NP.

Fig. 10 shows traces of the CO_2 formation rate (μmol g^{-1} s^{-1}) obtained during temperature-programmed oxidation (TPO) of the carbon accumulated after 12 h of DRM at 700 °C (20% CH_4/20% CO_2/He) over the two Ni/CeO_2 catalysts. The Ni/CeO_2-NP shows only a single peak at ~ 600 °C as opposed to the Ni/CeO_2-NR catalyst, where a main peak at ~ 580 °C, and a second smaller one at ~ 200 °C were observed. Shen et al. [113] reported that Pt supported on CeO_2 nanorods exhibited prominent carbon tolerance following 10-h DRM (CH_4: CO_2: N_2 = 1: 1: 3), where the amount of carbon deposited followed the order: Pt-CeO_2-NR (rods) (4.5 wt%) < Pt-CeO_2-NC (cubes) (9.4 wt%) < Pt-CeO_2-NP (polyhedra) (13.5 wt%). Ni/CeO_2-NC was found to accumulate large amounts of graphitic-type carbon that encapsulated Ni particles at the tail end, as opposed to the Ni/CeO_2-NR (nanorods) at 700 °C (50% CH_4/50% CO_2) [117]. The different morphology of CeO_2 support significantly affected not only the rate of carbon accumulation

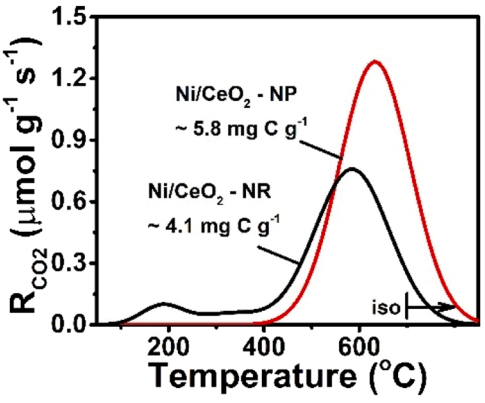

Fig. 10. CO_2 rate profiles (μmol g^{-1} s^{-1}) of carbon oxidation obtained during TPO for Ni/CeO_2-NP and Ni/CeO_2-NR following 12 h of DRM at 700 °C.

but also its structure. In the present work (Fig. 10), the shape and position of CO_2-TPO traces probes for different structures of carbon deposited as a function of CeO_2 support morphology. In this regard, inactive carbon in the form of graphite whiskers, carbon fibers and amorphous carbon has been identified over similar ceria-based catalytic systems [23,66,121,122]. For instance, carbon filaments and thin layers of graphitic carbon were identified over 5 wt% $Ni/Ce_{0.8}Pr_{0.2}O_{2-\delta}$ (0.22 wt% C, $d_{Ni} \sim 34$ nm) after DRM reaction at 750 °C for 25 h. The formation and removal rates of carbon can be affected by several factors, such as the Ni and ceria particle sizes, diffusion of carbon from the metal to the metal-support interface, as well as lattice oxygen diffusion towards the metal-support interface [23,25,64,122,125]. The lower amount of carbon (~ 40%) accumulated during DRM at 700 °C on Ni/CeO_2-NR compared to Ni/CeO_2-NP is considered as one of the reasons for the better catalytic performance of the former catalyst (Fig. 9 and Table S5).

3.6. *Quantification of CeO_2 lattice oxygen participation in the oxidation of carbon formed during DRM – Use of $^{18}O_2$*

The participation of lattice oxygen of bare CeO_2 and doped-CeO_2 carriers in supported Ni catalysts towards oxidation of carbon formed during DRM was quantified *for the first time* by our group using advanced transient isotopic experiments [25]. In the present work, the same experimental methodology was applied (see Section 2.4) to quantify the effect of CeO_2 morphology (shape) on the carbon oxidation path by lattice oxygen participation to be compared with the alternative one, that by oxygen derived from the CO_2 activation path. $^{16}O/^{18}O$ isotopic exchange was first performed at 700 °C for 10 min (use of 2% $^{18}O_2$/Ar) resulting in the exchange of a large number of ^{16}O layers (~ 80% of ^{16}O in the ceria structure - surface and bulk) for ^{18}O. During this $^{18}O_2$ gas treatment, oxidation of Ni to $Ni^{18}O$ occurred. The amount of oxygen exchanged in the CeO_2-NR and CeO_2-NP solids was very similar, ca. ~ 12 mmol O g^{-1} (after subtracting the ^{18}O present in $Ni^{18}O$). It should be noted that under the applied $^{16}O/^{18}O$ exchange reaction temperature of 700 °C, practically no -OH groups on the two ceria surfaces is expected [126].

Fig. 11**A** presents the dynamic evolution of $C^{18}O$ and $C^{16}O$ formation rates on Ni/CeO_2-NR and Ni/CeO_2-NP obtained at the step-gas switch He → 20% CH_4/20% CO_2/1% Kr/He (t) at 700 °C (see Section 2.4). The transient response curve of $C^{18}O$(g) is due to the reaction between the $^{18}O_L$ of support and the ^{12}C formed after the switch to the DRM gas mixture (mainly from $^{12}CH_4$ decomposition). The $C^{16}O$(g) transient response is due to the oxidation of carbon by oxygen species derived from the $C^{16}O_2$ activation route during the DRM reaction [25]. After ~ 65 s in DRM, the $C^{18}O$(g) formation ceases completely, while that of $C^{16}O$(g) reaches a steady state as expected. The shape of the transient rate of $C^{18}O$ and the time of appearance of peak maximum ($t_{max} \sim 7$ s) are very similar for the Ni/CeO_2-NR and Ni/CeO_2-NP, independent of CeO_2 morphology. On the other hand, the maximum value of the $C^{18}O$ (g) formation rate is different, with Ni/CeO_2-NR exhibiting a value ~ 1.5 times larger than that obtained on Ni/CeO_2-NP. The appearance of maximum in the $C^{18}O$ formation rate at the initial stage of the transient is an important parameter since at this stage of the transient, the source of ^{18}O is the first monolayer of surface lattice ^{18}O. As time goes by, the oxygen vacant sites formed are replenished by ^{16}O via $C^{16}O_2$ dissociation on V_O but also by ^{18}O via subsurface oxygen diffusion within the ceria solid towards the surface. The relative surface oxygen composition of ceria support until no $C^{18}O$(g) is observed would therefore depend on the relative rates of the above-mentioned reaction steps and that of carbon oxidation by the surface lattice oxygen of ceria.

The dynamic evolution of $C^{18}O$ and $C^{16}O$ formation rates for the Ni/

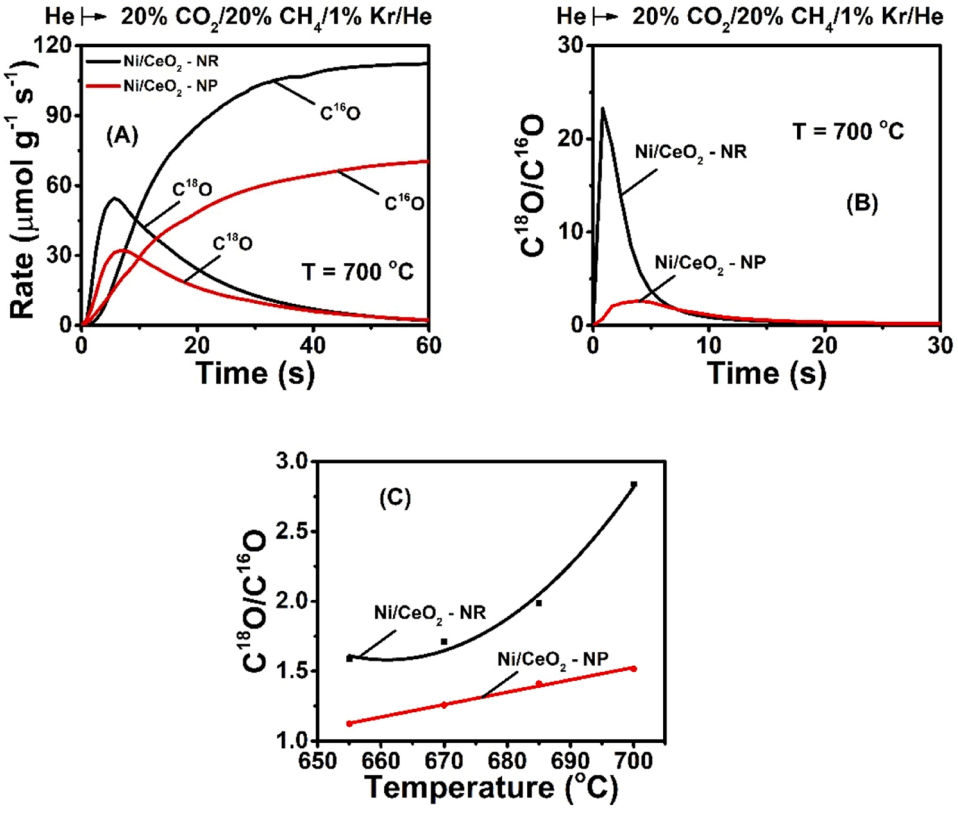

Fig. 11. (A) Dynamic rates of $C^{18}O$ and $C^{16}O$ formation (μmol g^{-1} s^{-1}) obtained during the step-gas switch He → 20% CO_2/20% CH_4/1% Kr/He (t) at 700 °C, following 10-min $^{18}O/^{16}O$ isotopic exchange over the two solids. (B) Ratio of normalized transient rates of $C^{18}O/C^{16}O$ as a function of time, and (C) Ratio of $C^{18}O$ and $C^{16}O$ formation rates at t= t_{max} (time of maximum appearance in the $C^{18}O$ formation rate). Experimental procedure: 20% O_2/He (700 °C, 2 h) → He (10 min) → 2% $^{18}O_2$/He (700 °C, 10 min) → He, cool down to 400 °C → H_2 (1 bar, 1 h) → He, increase T to 700 °C → DRM (700 °C, t).

CeO_2-NR and Ni/CeO_2-NP catalysts at lower reaction temperatures (655–685 °C) are depicted in Figures S3 and S4, respectively. It is evident that as the reaction temperature increases, the rate of carbon oxidation by the *lattice oxygen of ceria support* is favored over that of carbon oxidation by the oxygen derived from the CO_2 activation route. The dynamic behavior of the relative contribution of the two competitive carbon oxidation routes at 700 °C is depicted in Fig. 11**B**. It is illustrated that oxidation of carbon by the lattice oxygen of ceria prevails with respect to that by the oxygen derived from the CO_2 activation path. Additionally, the relative contribution of the two competitive routes of carbon oxidation to CO(g) at t_{max} (time at which the rate takes maximum value) in the 655–700 °C range is depicted in Fig. 11**C**. It is illustrated that the rate of carbon oxidation by ceria lattice oxygen is largely favored on Ni/CeO_2-NR at all temperatures, and its dependence on reaction T is different for the two CeO_2 morphologies (Fig. 11C, Table S6).

The amounts (μmol g^{-1}) of $C^{18}O$ formed during the transients shown in Fig. 11A and Figs S3 and S4 are reported in Table S6. It is important to point out that the equivalent ^{18}O amount (420–1200 μmol g^{-1}) corresponds to *several monolayers* of lattice oxygen in the CeO_2-NR and CeO_2-NP solids. This means that subsurface lattice oxygen can diffuse fast towards the surface and to subsequently react with carbon (formed on Ni surface and diffused towards the Ni-CeO_2 interface) to form CO(g) at 700 °C. As previously noted, the fact that no $H^{18}O$- hydroxyl groups are expected on the ceria surface at 700 °C, a likely formation of $HC^{18}OO$-s (formate) intermediate species during DRM able to get decomposed to $C^{18}O$ and H_2O (or H_2) should be excluded. Based on the transient $C^{18}O$ rate results at $t = t_{max}$ depicted in Fig. 11A and Figs S3-S4, an apparent activation energy for the oxidation of carbon by surface lattice ^{18}O of ceria support to $C^{18}O$(g) was estimated (Fig. 12**A**).

Similarly, based on the transient $C^{16}O$ rate results corresponding to the same reaction time ($t = t_{max}$), the apparent activation energy for the oxidation of carbon by oxygen derived from the CO_2 activation route on the Ni surface could be estimated, and results are shown in Fig. 12**B**. It is illustrated that surface labile lattice oxygen of both CeO_2 support morphologies provides an alternative and more energetically favourable path for carbon oxidation towards CO(g) under DRM reaction conditions. This alternative carbon oxidation path was found to depend on the morphology of nanoceria, where CeO_2-NR exhibits *lower* E_α (Fig. 12A, B). This result justifies the larger dynamic rates of $C^{18}O$ formation depicted in Fig. 11, and the lower amount of carbon accumulated after 12 h of DRM at 700 °C in comparison to the Ni/CeO_2-NP. For the oxidation of carbon by lattice oxygen, CeO_2-NR exhibits a value of E_a lower by 15 kJ mol^{-1} compared with the Ni/CeO_2-NP. It is suggested that this drop in activation energy relates more to the higher oxygen mobility on the surface of CeO_2-NR compared to CeO_2-NP as previously discussed. In the case of oxidation of carbon by oxygen species derived from the CO_2 dissociation on the Ni surface, a drop in E_a by 11 kJ mol^{-1} was obtained for CeO_2-NR compared to CeO_2-NP (Fig. 12B). This drop in E_a might partly be due to differences in the binding strength of carbon formed at Ni-ceria interfacial sites after CH_4 decomposition.

The origin of $C^{18}O$(g) formation rate depicted in Fig. 11, based on which it was possible to illustrate in a quantitative manner the importance of carbon oxidation by lattice oxygen, might be the result of a fast exchange of the ^{16}O of $C^{16}O_2$ with ^{18}O-$_L$ on the surface to form $C^{16}O^{18}O$ (after the switch He → CH_4/CO_2/He), followed by the reforming of $C^{16}O^{18}O$ with CH_4 [25]. To investigate this possibility on the present Ni/CeO_2 catalytic systems, the following experiment was conducted. After the $^{18}O_2$/Ar gas treatment of the catalyst at 700 °C followed by H_2 reduction at 400 °C (see Section 2.4), the step gas switch He → 10 or 20% CO_2/1% Kr/He was applied at 700 °C. Figure S5 depicts the transient rates (μmol g^{-1} s^{-1}) of $C^{16}O^{18}O$ and $C^{18}O_2$ obtained. It is worth mentioning that the rate of $C^{18}O$ formation was negligible compared to those of $C^{16}O^{18}O$ and $C^{18}O_2$ during the latter switch, suggesting that dissociation of $C^{18}O_2$ on the Ni metal surface and/or on ceria oxygen vacant sites was practically very small at the conditions of the experiment. The following should be noted:

(i) The transient evolution of $C^{16}O^{18}O$ and $C^{18}O_2$ formation rates appear practically proportional to the concentration of CO_2 used in the feed for both catalytic systems.

(ii) The time of appearance of maximum (t_{max}, s) in the dynamic rate of $C^{16}O^{18}O$ formation, the latter being significantly larger than that of $C^{18}O_2$ (Fig. S5), is larger compared to the value recorded for the $C^{18}O$(g) at the switch to the DRM gas mixture (Fig. 11A); 12.2 and 9.6 s for Ni/CeO_2-NP and Ni/CeO_2-NR, respectively (Fig. S5) compared to 7.3 and 5.7 s, respectively, under the DRM gas mixture (Fig. 11A).

(iii) If all $C^{16}O^{18}O$ and $C^{18}O_2$ produced during the 60-s transient period of CO_2 exchange with ^{18}O-$_L$ (Fig. S5) is considered to participate in the formation of $C^{18}O$ via DRM, then the sum of the corresponding transient rate curves of $C^{18}O$ can be compared to that of $C^{18}O$ measured at the switch to the DRM gas mixture (Fig. 11A). This comparison is illustrated in Fig. 13, where the $C^{18}O$(th1) and $C^{18}O$(th2) response curves refer to the theoretical scenario that all $C^{16}O^{18}O$ and $C^{18}O_2$ produced after exchange of $C^{16}O_2$ with ^{18}O-$_L$ react with CH_4 to form $C^{18}O$ and $C^{16}O$ (th1 curve: 20 vol% CO_2; th2 curve: 10 vol% CO_2 in the feed gas stream). It is seen that the experimental $C^{18}O$ response curve obtained at the switch to the DRM gas mixture is significantly larger than that of $C^{18}O$(th1) and $C^{18}O$(th2), and its maximum value is obtained at a shorter time.

(iv) The transient CO_2 concentration response curve obtained at the He → 20% CH_4/20% CO_2/He (700 °C, t) gas switch revealed that a steady-state rate of CO_2 conversion is obtained at ~ 8 s (20% CO_2 conversion in the case of Ni/CeO_2-NR). Thus, the concentration of CO_2 along the catalytic bed at the switch to the DRM

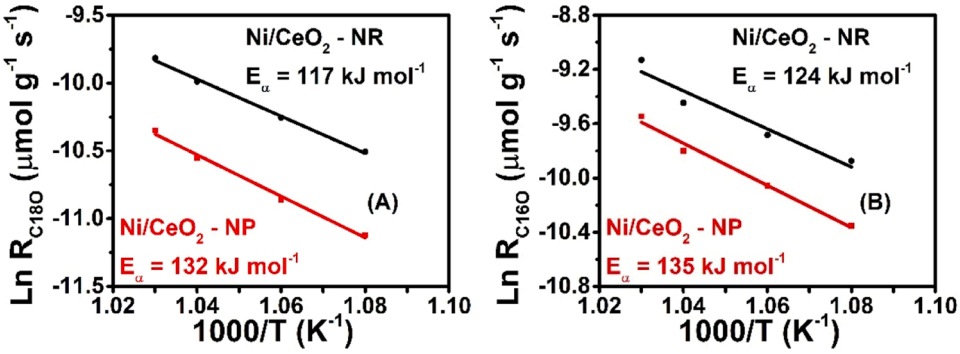

Fig. 12. Determination of the apparent activation energy (E_α, kJ mol^{-1}) of $C^{18}O$ (A) and $C^{16}O$ (B) formation due to the oxidation of carbon by the lattice oxygen of ceria support and by oxygen species derived via the CO_2 activation route, respectively, obtained under DRM reaction conditions (655−700 °C) following $^{16}O/^{18}O$ exchange (see Section 2.4).

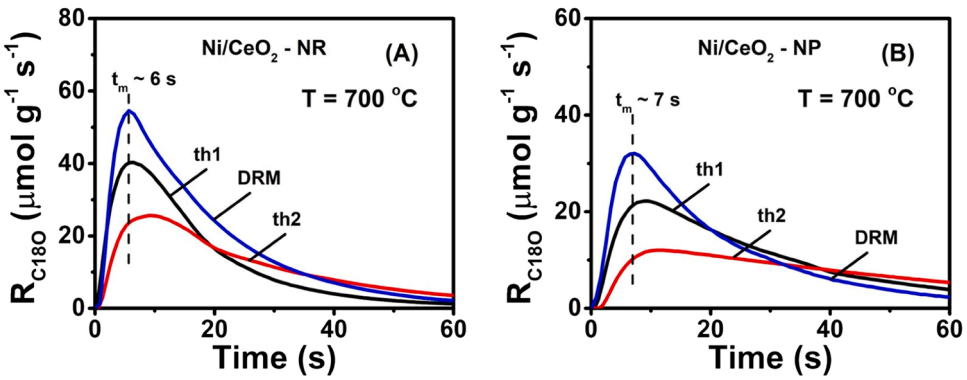

Fig. 13. Dynamic rates of $C^{18}O$ formation (μmol g^{-1} s^{-1}) obtained during the step-gas switches: (i) He → 20% CO_2/20% CH_4/1% Kr/He (t) (marked *DRM*), (ii) He → 20% CO_2/1%Kr/He (t) (marked *th1*), and (iii) He → 10% CO_2/1%Kr/He (t) (marked *th2*) at 700 °C, following 10-min $^{16}O/^{18}O$ isotopic exchange and H_2 reduction (see Section 2.4) over Ni/CeO_2-NR (A) and Ni/CeO_2-NP (B) catalysts.

reaction gas mixture (Fig. 11A) decreases progressively from 20 to 16 vol%. This result is very important since the $C^{18}O$ transient response curves marked th1 and th2 in Fig. 13 will be reduced by a factor of 1.25. Based on these results and the discussion provided, the ratio of the $C^{18}O$ to $C^{16}O$ initial formation rates depicted in Figs. 11B and 11C for t < 10 s must be considered largely unaffected by the possible dry reforming of $C^{16}O^{18}O$ and $C^{18}O_2$ with CH_4 to form $C^{16}O/C^{18}O$ and H_2. The latter confirms the significantly larger rate of carbon oxidation by the lattice oxygen of ceria than by oxygen species derived from the CO_2 dissociation step on the Ni surface and V_O sites.

3.7. Importance of morphology (shape) of ceria on the Ni/CeO_2 DRM activity

Ni/CeO_2 with two different morphologies of CeO_2 support (nanorods-NR and nanopolyhedra-NP) were synthesized aiming to investigate the effect of ceria morphology *(shape)* on important kinetic and other structural parameters that influence the DRM activity performance of Ni/CeO_2. In particular, the focus of the work was to correlate surface oxygen reduction rates, concentration of oxygen vacant sites, and lattice oxygen mobility with DRM activity (655–700 °C) as a function of ceria support morphology. The strong correlation of the activation energy for bulk oxygen diffusion with the rate of carbon oxidation to CO(g) by lattice oxygen measured under DRM (700 °C) for the two ceria support morphologies, is reported *for the first time* after using advanced transient ^{18}O isotopic experiments. The 5 wt% Ni supported on CeO_2-NR presents a lower activation energy (by ~8 kJ mol^{-1}) for surface oxygen reduction by hydrogen, significantly lower activation energy (by ~90 kJ mol^{-1}) for bulk oxygen diffusion, and a lower activation energy (by ~15 kJ mol^{-1}) for carbon oxidation by lattice oxygen leading to the formation of CO(g) under DRM (700 °C) compared to the 5 wt% Ni supported on CeO_2-NP. We have shown that Ni/CeO_2-NR presents a lower activation energy barrier (by ~11 kJ mol^{-1}) compared to Ni/CeO_2-NP for the oxidation of carbon to CO(g) by oxygen supplied after CO_2 dissociation on the Ni metal surface under DRM reaction conditions. Furthermore, evidence was given that CO_2 dissociation on reduced CeO_2-NR (V_O present) must be considered faster than on CeO_2-NP.

Table 2 compares in a comprehensive manner all the above mentioned kinetic and some other structural parameters of the Ni/CeO_2-NR and Ni/CeO_2-NP catalytic systems. The provided fundamental information via carefully designed transient kinetic and isotopic experiments resulted in the advancement of our understanding towards intrinsic kinetic reasons responsible for the significant enhancement of DRM activity in the 655–700 °C range of Ni supported on CeO_2-nanorods compared to CeO_2-nanopolyhedra. The experimental methodology followed in the present work paved the way for similar studies on other reactions over reducible metal oxides-supported catalysts, aiming to establish relationships between support morphology and kinetic parameters of relevant reaction steps.

Table 2
Comparison of important kinetic and structural parameters related to the Dry Reforming of Methane reaction on 5 wt% Ni supported on CeO_2-NR and CeO_2-NP.

Parameter	Ni/CeO_2 - NR	Ni/CeO_2 - NP
Percentage (%) of ceria reduction by H_2 at 700 °C	2.6	0.8
Apparent activation energy, E_α for surface O_L reduction by hydrogen (kJ mol^{-1})	51	59
Oxygen exchange (μmol O g^{-1}) at 640 °C	7.8	2.4
Apparent activation energy, E_b for bulk O_L diffusion (kJ mol^{-1})	245	334
Total surface basic sites (μmol g^{-1})	77.1	28.8
TOF_{CH4} (s^{-1}) of DRM reaction at 700 °C	0.44	0.21
Apparent activation energy, E_α for CH_4 conversion during DRM (kJ mol^{-1})	133	144
Amount of carbon accumulation after 12 h DRM at 700 °C (mg C g^{-1})	4.1	5.8
Relative importance of carbon oxidation by lattice oxygen of ceria support vs oxygen derived from CO_2 ($C^{18}O/C^{16}O$ ratio)	2.8	1.5
E_α - carbon oxidation by O_L of ceria support (kJ mol^{-1})	117	132
E_α - carbon oxidation by O_s derived from CO_2 dissociation (kJ mol^{-1})	124	135

4. Conclusions

In the present study, we delved into the intriguing interplay between CeO_2 support morphology (shape) and important kinetic parameters that control the activity of Ni/CeO_2 catalysts for the dry reforming of methane (DRM). By synthesizing CeO_2 in the form of nanorods (NR) and nanopolyhedra (NP), we uncovered compelling insights for the role of ceria morphology on critical kinetic parameters and aspects of the DRM reaction (e.g., resistance to carbon accumulation) in the 655–700 °C range. The essence of our findings lies in the profound impact of catalyst support morphology on the activation energy barriers associated with surface oxygen reduction and bulk oxygen diffusion of ceria, and their influence on the oxidation of carbon (formed mainly by CH_4 decomposition) by ceria lattice oxygen to form CO(g). The Ni/CeO_2-NR catalyst displayed a remarkable performance advantage over its Ni/CeO_2-NP counterpart, marked by lower activation energies in multiple key determined reaction steps. Specifically, it exhibited a 10 kJ mol^{-1} decrease in the activation energy for surface oxygen reduction with hydrogen, nearly 90 kJ mol^{-1} reduction in the activation energy for bulk oxygen diffusion, and a 15 kJ mol^{-1} drop in the activation energy

for carbon oxidation to CO(g) by the participation of the lattice oxygen of ceria. Moreover, a lower activation energy by 11 kJ mol^{-1} for the carbon oxidation to CO by oxygen species derived from CO_2 dissociation on the Ni metal surface was observed on Ni/CeO_2-NR compared to Ni/CeO_2-NP.

Our study underscored the pivotal role of oxygen mobility within the CeO_2 bulk structure in catalytic reactions, reminiscent of the influence of oxygen vacancy clusters and defects on carbon oxidation at the surface of CeO_2 nanorods. This superior oxygen mobility, coupled with a higher reducibility and a greater concentration of oxygen vacant sites formed in Ni/CeO_2-NR, provided compelling rationales for the enhanced DRM performance obtained. Specifically, it led to enhanced carbon gasification rates favouring CO production and a concomitant reduction in carbon accumulation (ca. by 30%), thus contributing to higher kinetic rates during DRM within the temperature range investigated. In summary, this study illuminates the pivotal role played by the ceria support morphology used in Ni/CeO_2 for the DRM reaction. These findings not only deepen our understanding of DRM conducted on Ni/CeO_2 of different support morphologies (nanorods vs nanopolyhedra) but offer also valuable insights for the design and optimization of other promising DRM catalytic systems based on reducible metal oxides as carriers of Ni and other metals.

CRediT authorship contribution statement

Soghomon Boghosian: Writing – review & editing, Supervision, Resources. **Theocharis Kentri:** Validation, Investigation, Formal analysis, Data curation. **Vassilios D. Binas:** Validation, Investigation, Formal analysis, Data curation. **Sofia Stefa:** Validation, Investigation, Formal analysis, Data curation. **Angelos M Efstathiou:** Writing – review & editing, Visualization, Supervision, Resources, Project administration, Methodology, Conceptualization. **Michalis Konsolakis:** Writing – review & editing, Visualization, Supervision, Resources, Project administration. **Maria Lykaki:** Validation, Investigation, Formal analysis, Data curation. **Constantinos M. Damaskinos:** Validation, Investigation, Formal analysis, Data curation. **Michalis A. Vasiliades:** Writing – original draft, Visualization, Validation, Methodology, Investigation, Formal analysis, Data curation.

Declaration of Competing Interest

The authors declare that they have no known competing financial interests or personal relationships that could have appeared to influence the work reported in this paper.

Data Availability

Data will be made available on request.

Acknowledgements

AME and MAV acknowledge the Research Committee of the University of Cyprus, SB and TK the Research Committee of the University of Patras, and MK the Technical University of Crete and the European Union (project code: TAEDK-06169) for financial support.

Appendix A. Supporting information

Supplementary data associated with this article can be found in the online version at doi:10.1016/j.apcatb.2024.123906.

References

[1] Z. Bian, S. Das, M.H. Wai, P. Hongmanorom, S. Kawi, A review on bimetallic nickel-based catalysts for CO_2 reforming of methane, ChemPhysChem 18 (2017) 3117–3134, https://doi.org/10.1002/cphc.201700529.

[2] J.M. Lavoie, Review on dry reforming of methane, a potentially more environmentally-friendly approach to the increasing natural gas exploitation, Front. Chem. 2 (2014), https://doi.org/10.3389/fchem.2014.00081.

[3] M.M. Zain, A.R. Mohamed, An overview on conversion technologies to produce value added products from CH_4 and CO_2 as major biogas constituents, Renew. Sustain. Energy Rev. 98 (2018) 56–63, https://doi.org/10.1016/j.rser.2018.09.003.

[4] D.B.L. Santos, F.B. Noronha, C.E. Hori, Bi-reforming of methane for hydrogen production using $LaNiO_3/Ce_xZr_{1-x}O_2$ as precursor material, Int. J. Hydrog. Energy 45 (2020) 13947–13959, https://doi.org/10.1016/j.ijhydene.2020.03.096.

[5] S. Arora, R. Prasad, An overview on dry reforming of methane: Strategies to reduce carbonaceous deactivation of catalysts, RSC Adv. 6 (2016) 108668–108688, https://doi.org/10.1039/c6ra20450c.

[6] A.G.S. Hussien, K. Polychronopoulou, A Review on the Different Aspects and Challenges of the Dry Reforming of Methane (DRM) Reaction, Nanomaterials 12 (2022) 3400, https://doi.org/10.3390/nano12193400.

[7] D. Pakhare, J. Spivey, A review of dry (CO_2) reforming of methane over noble metal catalysts, Chem. Soc. Rev. 43 (2014) 7813–7837, https://doi.org/10.1039/c3cs60395d.

[8] G. Zhang, J. Liu, Y. Xu, Y. Sun, A review of CH_4–CO_2 reforming to synthesis gas over Ni-based catalysts in recent years (2010–2017), Int. J. Hydrog. Energy 43 (2018) 15030–15054, https://doi.org/10.1016/j.ijhydene.2018.06.091.

[9] Z. Alipour, V. Babu Borugadda, H. Wang, A.K. Dalai, Syngas production through dry reforming: A review on catalysts and their materials, preparation methods and reactor type, Chem. Eng. J. 452 (2023) 139416, https://doi.org/10.1016/j.cej.2022.139416.

[10] M. Boaro, S. Colussi, A. Trovarelli, Ceria-based materials in hydrogenation and reforming reactions for CO_2 valorization, Front. Chem. 7 (2019), https://doi.org/10.3389/fchem.2019.00028.

[11] P.G. Lustemberg, P.J. Ramírez, Z. Liu, R.A. Gutiérrez, D.G. Grinter, J. Carrasco, S. D. Senanayake, J.A. Rodriguez, M.V. Ganduglia-Pirovano, Room-temperature activation of methane and dry re-forming with CO_2 on Ni-CeO_2(111) surfaces: effect of Ce^{3+} sites and metal-support interactions on C-H bond cleavage, ACS Catal. 6 (2016) 8184–8191, https://doi.org/10.1021/acscatal.6b02360.

[12] S. Kawi, Y. Kathiraser, J. Ni, U. Oemar, Z. Li, E.T. Saw, Progress in synthesis of highly active and stable nickel-based catalysts for carbon dioxide reforming of methane, ChemSusChem 8 (2015) 3556–3575, https://doi.org/10.1002/cssc.201500390.

[13] S.B. Kim, A.A.S. Eissa, M.J. Kim, E.S. Goda, J.R. Youn, K. Lee, Sustainable synthesis of a highly stable and coke-free Ni@CeO_2 catalyst for the efficient carbon dioxide reforming of methane, Catalysts 12 (2022), https://doi.org/10.3390/catal12040423.

[14] J.W. Han, J.S. Park, M.S. Choi, H. Lee, Uncoupling the size and support effects of Ni catalysts for dry reforming of methane, Appl. Catal. B Environ. 203 (2017) 625–632, https://doi.org/10.1016/j.apcatb.2016.10.069.

[15] Z. Lian, S.O. Olanrele, C. Si, M. Yang, B. Li, Critical role of interfacial sites between nickel and CeO_2 support in dry reforming of methane: revisit of reaction mechanism and origin of stability, J. Phys. Chem. C 124 (2020) 5118–5124, https://doi.org/10.1021/acs.jpcc.9b09856.

[16] W.N. Manan, W.N.R. Wan Isahak, Z. Yaakob, CeO_2-based heterogeneous catalysts in dry reforming methane and steam reforming methane: a short review, Catalysts 12 (2022) 452, https://doi.org/10.3390/catal12050452.

[17] I.C. Sophiana, F. Iskandar, H. Devianto, N. Nishiyama, Y.W. Budhi, Coke-resistant Ni/$CeZrO_2$ catalysts for dry reforming of methane to produce hydrogen-rich syngas, Nanomaterials 12 (2022), https://doi.org/10.3390/nano12091556.

[18] E. Smal, Y. Bespalko, M. Arapova, V. Fedorova, K. Valeev, N. Eremeev, E. Sadovskaya, T. Krieger, T. Glazneva, V. Sadykov, M. Simonov, Carbon formation during methane dry reforming over Ni-containing ceria-zirconia catalysts, Nanomaterials 12 (2022), https://doi.org/10.3390/nano12203676.

[19] L.P. Teh, H.D. Setiabudi, S.N. Timmiati, M.A.A. Aziz, N.H.R. Annuar, N.N. Ruslan, Recent progress in ceria-based catalysts for the dry reforming of methane: a review, Chem. Eng. Sci. 242 (2021) 116606, https://doi.org/10.1016/j.ces.2021.116606.

[20] C. Vogt, J. Kranenborg, M. Monai, B.M. Weckhuysen, Structure sensitivity in steam and dry methane reforming over nickel: activity and carbon formation, ACS Catal. 10 (2020) 1428–1438, https://doi.org/10.1021/acscatal.9b04193.

[21] I. Luisetto, S. Tuti, C. Romano, M. Boaro, E. Di Bartolomeo, Dry reforming of methane over Ni supported on doped CeO_2: new insight on the role of dopants for CO_2 activation, J. CO_2 Util. 30 (2019) 63–78, https://doi.org/10.1016/j.jcou.2019.01.006.

[22] Y. Lyu, J. Jocz, R. Xu, E. Stavitski, C. Sievers, Nickel speciation and methane dry reforming performance of Ni/$Ce_xZr_{1-x}O_2$ prepared by different synthesis methods, ACS Catal. 10 (2020) 11235–11252, https://doi.org/10.1021/acscatal.0c02426.

[23] A.G.S. Hussien, C.M. Damaskinos, A. Dabbawala, D.H. Anjum, M.A. Vasiliades, M. T.A. Khaleel, N. Wehbe, A.M. Efstathiou, K. Polychronopoulou, Elucidating the role of La^{3+}/Sm^{3+} in the carbon paths of dry reforming of methane over Ni/Ce-La (Sm)-Cu-O using transient kinetics and isotopic techniques, Appl. Catal. B Environ. 304 (2022) 121015, https://doi.org/10.1016/j.apcatb.2021.121015.

[24] S. Tuti, I. Luisetto, U. Pasqual Laverdura, E. Marconi, Dry reforming of methane on Ni/nanorod-CeO_2 catalysts prepared by one-pot hydrothermal synthesis: the effect of Ni content on structure, activity, and stability, Reactions 3 (2022) 333–351, https://doi.org/10.3390/reactions3030025.

[25] C.M. Damaskinos, J. Zavašnik, P. Djinović, A.M. Efstathiou, Dry reforming of methane over $Ni/Ce_{0.8}Ti_{0.2}O_{2-\delta}$: the effect of Ni particle size on the carbon pathways studied by transient and isotopic techniques, Appl. Catal. B Environ. 296 (2021), https://doi.org/10.1016/j.apcatb.2021.120321.

[26] Z. Wu, M. Li, J. Howe, H.M.I.I.I. Meyer, S.H. Overbury, Probing defect sites on CeO_2nanocrystals with well-defined surface planes by Raman spectroscopy and O_2 adsorption, Langmuir 26 (2010) 16595–16606, https://doi.org/10.1021/la101723w.

[27] E. Aneggi, D. Wiater, C. de Leitenburg, J. Llorca, A. Trovarelli, Shape-dependent activity of ceria in soot combustion, ACS Catal. 4 (2014) 172–181, https://doi.org/10.1021/cs400850r.

[28] M. Piumetti, S. Bensaid, T. Andana, M. Dosa, C. Novara, F. Giorgis, N. Russo, D. Fino, Nanostructured ceria-based materials: effect of the hydrothermal synthesis conditions on the structural properties and catalytic activity, Catalysts 7 (2017), https://doi.org/10.3390/catal7060174.

[29] S. Gao, Y. Li, W. Guo, X. Ding, L. Zheng, L. Wu, H. Yan, Y. Wang, Morphology effect of ceria support with hierarchical structure on the catalytic performance for nickel-based catalysts in dry reforming of methane, Mol. Catal. 533 (2022) 112766, https://doi.org/10.1016/j.mcat.2022.112766.

[30] S.C. Rood, H.B. Ahmet, A. Gomez-Ramon, L. Torrente-Murciano, T.R. Reina, S. Eslava, Enhanced ceria nanoflakes using graphene oxide as a sacrificial template for CO oxidation and dry reforming of methane, Appl. Catal. B Environ. 242 (2019) 358–368, https://doi.org/10.1016/j.apcatb.2018.10.011.

[31] S.J. Hassani Rad, M. Haghighi, A. Alizadeh Eslami, F. Rahmani, N. Rahemi, Sol–gel vs. impregnation preparation of MgO and CeO_2 doped Ni/Al_2O_3 nanocatalysts used in dry reforming of methane: Effect of process conditions, synthesis method and support composition, Int. J. Hydrog. Energy 41 (2016) 5335–5350, https://doi.org/10.1016/j.ijhydene.2016.02.002.

[32] F. Zhang, Z. Liu, X. Chen, N. Rui, L.E. Betancourt, L. Lin, W. Xu, C.J. Sun, A.M. M. Abeykoon, J.A. Rodriguez, J. Teržan, K. Lorber, P. Djinović, S.D. Senanayake, Effects of Zr Doping Into Ceria For The Dry Reforming Of Methane Over Ni/$CeZrO_2$ Catalysts: In Situ Studies With XRD, XAFS, and AP-XPS, ACS Catal. 10 (2020) 3274–3284, https://doi.org/10.1021/acscatal.9b04451.

[33] A. Álvarez Moreno, T. Ramirez-Reina, S. Ivanova, A.-C. Roger, M.Á. Centeno, J. A. Odriozola, Bimetallic Ni–Ru and Ni–Re Catalysts For Dry Reforming Of Methane: Understanding The Synergies Of The Selected Promoters, Front. Chem. 9 (2021), https://doi.org/10.3389/fchem.2021.694976.

[34] A. Trovarelli, J. Llorca, Ceria Catalysts At Nanoscale: How Do Crystal Shapes Shape Catalysis? ACS Catal. 7 (2017) 4716–4735, https://doi.org/10.1021/acscatal.7b01246.

[35] M. Melchionna, P. Fornasiero, The role of ceria-based nanostructured materials in energy applications, Mater. Today 17 (2014) 349–357, https://doi.org/10.1016/j.mattod.2014.05.005.

[36] T. Montini, M. Melchionna, M. Monai, P. Fornasiero, Fundamentals and Catalytic Applications of CeO_2-Based Materials, Chem. Rev. 116 (2016) 5987–6041, https://doi.org/10.1021/acs.chemrev.5b00603.

[37] J.A. Rodriguez, D.C. Grinter, Z. Liu, R.M. Palomino, S.D. Senanayake, Ceria-based model catalysts: Fundamental studies on the importance of the metal-ceria interface in CO oxidation, the water-gas shift, CO_2 hydrogenation, and methane and alcohol reforming, Chem. Soc. Rev. 46 (2017) 1824–1841, https://doi.org/10.1039/c6cs00863a.

[38] K. Wu, L.D. Sun, C.H. Yan, Recent Progress In Well-controlled Synthesis Of Ceria-based Nanocatalysts Towards Enhanced Catalytic Performance, Adv. Energy Mater. 6 (2016) 1–46, https://doi.org/10.1002/aenm.201600501.

[39] M. Cargnello, V.V.T. Doan-Nguyen, T.R. Gordon, R.E. Diaz, E.A. Stach, R.J. Gorte, P. Fornasiero, C.B. Murray, Control of metal nanocrystal size reveals metal-support interface role for ceria catalysts, Science 341 (2013) 771–773, https://doi.org/10.1126/science.1240148.

[40] E.D. Hermes, G.R. Jenness, J.R. Schmidt, Decoupling the electronic, geometric and interfacial contributions to support effects in heterogeneous catalysis, Mol. Simul. 41 (2015) 123–133, https://doi.org/10.1080/08927022.2014.926549.

[41] S. Mitchell, R. Qin, N. Zheng, J. Pérez-Ramírez, Nanoscale engineering of catalytic materials for sustainable technologies, Nat. Nanotechnol. 16 (2021) 129–139, https://doi.org/10.1038/s41565-020-00799-8.

[42] A.R. Puigdollers, P. Schlexer, S. Tosoni, G. Pacchioni, Increasing oxide reducibility: The role of metal/oxide interfaces in the formation of oxygen vacancies, ACS Catal. 7 (2017) 6493–6513, https://doi.org/10.1021/acscatal.7b01913.

[43] M. Konsolakis, The role of Copper–Ceria interactions in catalysis science: Recent theoretical and experimental advances, Appl. Catal. B Environ. 198 (2016) 49–66, https://doi.org/10.1016/j.apcatb.2016.05.037.

[44] H. Mistry, F. Behafarid, R. Reske, A.S. Varela, P. Strasser, B. Roldan Cuenya, Tuning Catalytic Selectivity At The Mesoscale Via Interparticle Interactions, ACS Catal. 6 (2016) 1075–1080, https://doi.org/10.1021/acscatal.5b02202.

[45] T.W. van Deelen, C. Hernández Mejía, K.P. de Jong, Control of metal-support interactions in heterogeneous catalysts to enhance activity and selectivity, Nat. Catal. 2 (2019) 955–970, https://doi.org/10.1038/s41929-019-0364-x.

[46] M. Capdevila-Cortada, G. Vilé, D. Teschner, J. Pérez-Ramírez, N. López, Reactivity descriptors for ceria in catalysis, Appl. Catal. B Environ. 197 (2016) 299–312, https://doi.org/10.1016/j.apcatb.2016.02.035.

[47] M. Ahmadi, H. Mistry, B. Roldan Cuenya, Tailoring the catalytic properties of metal nanoparticles via support interactions, J. Phys. Chem. Lett. 7 (2016) 3519–3533, https://doi.org/10.1021/acs.jpclett.6b01198.

[48] Y. Wang, R. Zhang, B. Yan, Ni/$Ce_{0.9}Eu_{0.1}O_{1.95}$ with enhanced coke resistance for dry reforming of methane, J. Catal. 407 (2022) 77–89, https://doi.org/10.1016/j.jcat.2022.01.020.

[49] L. Liu, A. Corma, Metal catalysts for heterogeneous catalysis: from single atoms to nanoclusters and nanoparticles, Chem. Rev. 118 (2018) 4981–5079, https://doi.org/10.1021/acs.chemrev.7b00776.

[50] M. Konsolakis, Z. Ioakeimidis, Surface/structure functionalization of copper-based catalysts by metal-support and/or metal-metal interactions, Appl. Surf. Sci. 320 (2014) 244–255, https://doi.org/10.1016/j.apsusc.2014.08.114.

[51] M. Konsolakis, M. Lykaki, Recent advances on the rational design of nonprecious metal oxide catalysts exemplified by CuO_x/CoO_2 binary system: Implications of size, shape and electronic effects on intrinsic reactivity and metal-support interactions, Catalysts 10 (2020) 160, https://doi.org/10.3390/catal10020160.

[52] G. Varvoutis, M. Lykaki, S. Stefa, V. Binas, G.E. Marnellos, M. Konsolakis, Deciphering the role of Ni particle size and nickel-ceria interfacial perimeter in the low-temperature CO_2 methanation reaction over remarkably active Ni/CeO_2 nanorods, Appl. Catal. B Environ. 297 (2021) 120401, https://doi.org/10.1016/j.apcatb.2021.120401.

[53] G. Varvoutis, M. Lykaki, S. Stefa, E. Papista, S.A.C. Carabineiro, G.E. Marnellos, M. Konsolakis, Remarkable efficiency of Ni supported on hydrothermally synthesized CeO_2 nanorods for low-temperature CO_2 hydrogenation to methane, Catal. Commun. 142 (2020) 106036, https://doi.org/10.1016/j.catcom.2020.106036.

[54] M. Konsolakis, M. Lykaki, Facet-dependent reactivity of ceria nanoparticles exemplified by CeO_2-based transition metal catalysts: a critical review, Catalysts 11 (2021), https://doi.org/10.3390/catal11040452.

[55] M. Konsolakis, M. Lykaki, S. Stefa, S.A.C. Carabineiro, G. Varvoutis, E. Papista, G. E. Marnellos, CO_2 hydrogenation over nanoceria-supported transition metal catalysts: role of ceria morphology (nanorods versus nanocubes) and active phase nature (Co versus Cu), Nanomaterials 9 (2019) 1739, https://doi.org/10.3390/nano9121739.

[56] M. Lykaki, E. Pachatouridou, S.A.C. Carabineiro, E. Iliopoulou, C. Andriopoulou, N. Kallithrakas-Kontos, S. Boghosian, M. Konsolakis, Ceria nanoparticles shape effects on the structural defects and surface chemistry: implications in CO oxidation by Cu/CeO_2 catalysts, Appl. Catal. B Environ. 230 (2018) 18–28, https://doi.org/10.1016/j.apcatb.2018.02.035.

[57] M. Lykaki, E. Papista, N. Kaklidis, S.A.C. Carabineiro, M. Konsolakis, Ceria nanoparticles' morphological effects on the N_2O decomposition performance of Co_3O_4/CeO_2 mixed oxides, Catalysts 9 (2019) 233, https://doi.org/10.3390/catal9030233.

[58] M. Lykaki, S. Stefa, S.A.C. Carabineiro, P.K. Pandis, V.N. Stathopoulos, M. Konsolakis, Facet-dependent reactivity of Fe_2O_3/CeO_2 nanocomposites: Effect of ceria morphology on CO oxidation, Catalysts 9 (2019) 371, https://doi.org/10.3390/catal9040371.

[59] S. Stefa, M. Lykaki, V. Binas, P.K. Pandis, V.N. Stathopoulos, M. Konsolakis, Hydrothermal synthesis of ZnO–doped ceria nanorods: Effect of ZnO content on the redox properties and the CO oxidation performance, Appl. Sci. 10 (2020) 1–13, https://doi.org/10.3390/app10217605.

[60] S. Stefa, M. Lykaki, D. Fragkoulis, V. Binas, P.K. Pandis, V.N. Stathopoulos, M. Konsolakis, Effect of the preparation method on the physicochemical properties and the CO oxidation performance of nanostructured CeO_2/TiO_2 oxides, Processes 8 (2020) 847, https://doi.org/10.3390/pr8070847.

[61] G. Varvoutis, S.A. Karakoulia, M. Lykaki, S. Stefa, V. Binas, G.E. Marnellos, M. Konsolakis, Support-induced modifications on the CO_2 hydrogenation performance of Ni/CeO_2: The effect of ZnO doping on CeO_2 nanorods, J. CO_2 Util. 61 (2022), https://doi.org/10.1016/j.jcou.2022.102057.

[62] M.A. Vasiliades, C.M. Damaskinos, P. Djinović, A. Pintar, A.M. Efstathiou, Dry reforming of CH_4 over NiCo/$Ce_{0.75}Zr_{0.25}O_{2-\delta}$: The effect of Co on the site activity and carbon pathways studied by transient techniques, Catal. Commun. 149 (2021) 106237, https://doi.org/10.1016/j.catcom.2020.106237.

[63] M.A. Vasiliades, P. Djinović, L.F. Davlyatova, A. Pintar, A.M. Efstathiou, Origin and reactivity of active and inactive carbon formed during DRM over Ni/$Ce_{0.38}Zr_{0.62}O_{2-\delta}$ studied by transient isotopic techniques, Catal. Today 299 (2018) 201–211, https://doi.org/10.1016/j.cattod.2017.03.057.

[64] C.M. Damaskinos, M.A. Vasiliades, V.N. Stathopoulos, A.M. Efstathiou, The effect of CeO_2 preparation method on the carbon pathways in the dry reforming of methane on Ni/CeO_2 studied by transient techniques, Catalysts 9 (2019) 621, https://doi.org/10.3390/catal9070621.

[65] C.M. Damaskinos, M.A. Vasiliades, A.M. Efstathiou, The effect of Ti^{4+} dopant in the 5 wt% Ni/$Ce_{1-x}Ti_xO_{2-\delta}$ catalyst on the carbon pathways of dry reforming of methane studied by various transient and isotopic techniques, Appl. Catal. A Gen. 579 (2019) 116–129, https://doi.org/10.1016/j.apcata.2019.04.023.

[66] M.A. Vasiliades, M.M. Makri, P. Djinović, B. Erjavec, A. Pintar, A.M. Efstathiou, Dry reforming of methane over 5 wt% Ni/$Ce_{1-x}Pr_xO_{2-\delta}$ catalysts: Performance and characterisation of active and inactive carbon by transient isotopic techniques, Appl. Catal. B Environ. 197 (2016) 168–183, https://doi.org/10.1016/j.apcatb.2016.03.012.

[67] S. Damyanova, B. Pawelec, R. Palcheva, Y. Karakirova, M.C. Capel-Sanchez, G. Tyuliev, E. Gaigneaux, J.L.G. Fierro, Structure and surface properties of ceria-modified Ni-based catalysts for hydrogen production, Appl. Catal. B Environ. 225 (2018) 340–353, https://doi.org/10.1016/j.apcatb.2017.12.002.

[68] K. Lorber, J. Zavašnik, I. Arčon, M. Huš, J. Teržan, B. Likozar, P. Djinović, CO_2 Activation over Nanoshaped CeO_2 Decorated with Nickel for Low-Temperature Methane Dry Reforming, ACS Appl. Mater. Interfaces 14 (2022) 31862–31878, https://doi.org/10.1021/acsami.2c05221.

[69] P.G. Lustemberg, Z. Mao, A. Salcedo, B. Irigoyen, M.V. Ganduglia-Pirovano, C. T. Campbell, Nature of the active sites on Ni/CeO_2 catalysts for methane conversions, ACS Catal. 11 (2021) 10604–10613, https://doi.org/10.1021/acscatal.1c02154.

[70] X. Gao, P. Cai, Z. Wang, X. Lv, S. Kawi, Surface acidity/basicity and oxygen defects of metal oxide: impacts on catalytic performances of CO_2 reforming and

hydrogenation reactions, Top. Catal. 66 (2023) 299–325, https://doi.org/10.1007/s11244-022-01708-0.
[71] G. Tsilomelekis, S. Boghosian, On the configuration, molecular structure and vibrational properties of MoOx sites on alumina, zirconia, titania and silica, Catal. Sci. Technol. 3 (2013) 1869–1888, https://doi.org/10.1039/c3cy00057e.
[72] A. Christodoulakis, S. Boghosian, Molecular structure and activity of molybdena catalysts supported on zirconia for ethane oxidative dehydrogenation studied by operando Raman spectroscopy, J. Catal. 260 (2008) 178–187, https://doi.org/10.1016/j.jcat.2008.09.025.
[73] C. Andriopoulou, A. Trimpalis, K.C. Petallidou, A. Sgoura, A.M. Efstathiou, S. Boghosian, Structural and Redox Properties of $Ce_{1-x}Zr_xO_{2-\delta}$ and $Ce_{0.8}Zr_{0.15}RE_{0.05}O_{2-\delta}$ (RE: La, Nd, Pr, Y) Solids Studied by High Temperature in Situ Raman Spectroscopy, J. Phys. Chem. C. 121 (2017) 7931–7943, https://doi.org/10.1021/acs.jpcc.7b00515.
[74] C. Andriopoulou, D. Harris, H. Stephenson, A.M. Efstathiou, S. Boghosian, In situ Raman spectroscopy as a tool for discerning subtle structural differences between commercial (Ce, Zr)O_2-based OSC materials of identical composition, Catalysts 10 (2020), https://doi.org/10.3390/catal10040462.
[75] M.A. Vasiliades, D. Harris, H. Stephenson, S. Boghosian, A.M. Efstathiou, A Novel Analysis of Transient Isothermal ^{18}O Isotopic Exchange on Commercial $Ce_xZr_{1-x}O_2$-Based OSC Materials, Top. Catal. 62 (2019) 219–226, https://doi.org/10.1007/s11244-018-1116-x.
[76] A.M. Efstathiou, D. Papageorgiou, X.E. Verykios, The role of lattice oxygen during the oxidative coupling of methane over Li^+-Doped TiO_2 catalysts, J. Catal. 144 (1993) 352–357, https://doi.org/10.1006/jcat.1993.1336.
[77] K.P. Peil, J.G. Goodwin, G. Marcelin, Surface phenomena during the oxidative coupling of methane over Li/MgO, J. Catal. 131 (1991) 143–155, https://doi.org/10.1016/0021-9517(91)90331-W.
[78] M.A. Vasiliades, N.S. Govender, A. Govender, R. Crous, D. Moodley, T. Botha, A. M. Efstathiou, The effect of H_2 pressure on the carbon path of methanation reaction on Co/γ-Al_2O_3: transient isotopic and operando methodology studies, ACS Catal. 12 (2022) 15110–15129, https://doi.org/10.1021/acscatal.2c04269.
[79] M.A. Vasiliades, K.K. Kyprianou, N.S. Govender, A. Govender, R. Crous, D. Moodley, A.M. Efstathiou, The effect of CO partial pressure on important kinetic parameters of methanation reaction on Co- based FTS catalyst studied by SSITKA-MS and operando DRIFTS-MS techniques, Catalysts 10 (2020), https://doi.org/10.3390/catal10050583.
[80] M.A. Vasiliades, C.M. Kalamaras, N.S. Govender, A. Govender, A.M. Efstathiou, The effect of preparation route of commercial Co/γ-Al_2O_3 catalyst on important Fischer-Tropsch kinetic parameters studied by SSITKA and CO-DRIFTS transient hydrogenation techniques, J. Catal. 379 (2019) 60–77, https://doi.org/10.1016/j.jcat.2019.09.008.
[81] C. Perego, S. Peratello, Experimental methods in catalytic kinetics, Catal. Today 52 (1999) 133–145, https://doi.org/10.1016/S0920-5861(99)00071-1.
[82] R. Si, M. Flytzani-Stephanopoulos, Shape and crystal-plane effects of nanoscale ceria on the activity of Au-CeO_2 catalysts for the water-gas shift reaction, Angew. Chem. 120 (2008) 2926–2929, https://doi.org/10.1002/ange.200705828.
[83] C. Zhu, X. Wei, W. Li, Y. Pu, J. Sun, K. Tang, H. Wan, C. Ge, W. Zou, L. Dong, ACS Sustain. Chem. Eng. 8 (2020) 14397–14406, https://doi.org/10.1021/acssuschemeng.0c04205.
[84] Z. Wu, M. Li, J. Howe, H.M. Meyer, S.H. Overbury, Probing defect sites on CeO_2 nanocrystals with well-defined surface planes by raman spectroscopy and O_2 adsorption, Langmuir 26 (2010) 16595–16606, https://doi.org/10.1021/la101723w.
[85] E. Mamontov, T. Egami, R. Brezny, M. Koranne, S. Tyagi, Lattice defects and oxygen storage capacity of nanocrystalline ceria and ceria-zirconia, J. Phys. Chem. B 104 (2000) 11110–11116, https://doi.org/10.1021/jp0023011.
[86] Z. Qin, L. Chen, J. Chen, T. Su, H. Ji, Ni/CeO_2 prepared by improved polyol method for DRM with highly dispersed Ni, Greenh. Gases Sci. Technol. 11 (2021) 1245–1264, https://doi.org/10.1002/ghg.2129.
[87] W. Huang, Y. Gao, Morphology-dependent surface chemistry and catalysis of CeO_2 nanocrystals, Catal. Sci. Technol. 4 (2014) 3772–3784, https://doi.org/10.1039/c4cy00679h.
[88] C.T. Campbell, C.H.F. Peden, Oxygen Vacancies and Catalysis on Ceria Surfaces, Science 309 (2005) 713–714, https://doi.org/10.1126/science.1113955.
[89] F. Esch, S. Fabris, L. Zhou, T. Montini, C. Africh, P. Fornasiero, G. Comelli, R. Rosei, Electron Localization Determines Defect Formation on Ceria Substrates, Science 309 (2005) 752–755, https://doi.org/10.1126/science.1111568.
[90] L. Ilieva, P. Petrova, G. Pantaleo, R. Zanella, L.F. Liotta, V. Georgiev, S. Boghosian, Z. Kaszkur, J.W. Sobczak, W. Lisowski, A.M. Venezia, T. Tabakova, Gold catalysts supported on Y-modified ceria for CO-free hydrogen production via PROX, Appl. Catal. B Environ. 188 (2016) 154–168, https://doi.org/10.1016/j.apcatb.2016.02.004.
[91] S.Y. Christou, A.M. Efstathiou, The effects of P-poisoning of $Ce_xZr_{1-x}O_2$ on the transient oxygen storage and release kinetics, Top. Catal. 56 (2013) 232–238, https://doi.org/10.1007/s11244-013-9959-7.
[92] Y. Li, W. Shen, Morphology-dependent nanocatalysts: Rod-shaped oxides, Chem. Soc. Rev. 43 (2014) 1543–1574, https://doi.org/10.1039/c3cs60296f.
[93] Z. Ma, S. Zhao, X. Pei, X. Xiong, B. Hu, New insights into the support morphology-dependent ammonia synthesis activity of Ru/CeO_2 catalysts, Catal. Sci. Technol. 7 (2017) 191–199, https://doi.org/10.1039/c6cy02089e.
[94] P. Djinović, I.G. Osojnik Crnivec, B. Erjavec, A. Pintar, Influence of active metal loading and oxygen mobility on coke-free dry reforming of Ni-Co bimetallic catalysts, Appl. Catal. B Environ. 125 (2012) 259–270, https://doi.org/10.1016/j.apcatb.2012.05.049.
[95] K. Polychronopoulou, S. AlKhoori, S. AlBedwawi, S. Alareeqi, A.G.S. Hussien, M. A. Vasiliades, A.M. Efstathiou, K.C. Petallidou, N. Singh, D.H. Anjum, L.F. Vega, M.A. Baker, Decoupling the Chemical and Mechanical Strain Effect on Steering the CO_2 Activation over CeO_2-Based Oxides: An Experimental and DFT Approach, ACS Appl. Mater. Interfaces 14 (2022) 33094–33119, https://doi.org/10.1021/acsami.2c05714.
[96] K. Polychronopoulou, A.A. Alkhoori, A.M. Efstathiou, M.A. Jaoude, C. M. Damaskinos, M.A. Baker, A. Almutawa, D.H. Anjum, M.A. Vasiliades, A. Belabbes, L.F. Vega, A.F. Zedan, S.J. Hinder, Design aspects of doped CeO_2 for low-temperature catalytic CO oxidation: transient kinetics and DFT approach, ACS Appl. Mater. Interfaces 13 (2021) 22391–22415, https://doi.org/10.1021/acsami.1c02934.
[97] D.V. Ivanov, E.M. Sadovskaya, L.G. Pinaeva, L.A. Isupova, Influence of oxygen mobility on catalytic activity of La-Sr-Mn-O composites in the reaction of high temperature N_2O decomposition, J. Catal. 267 (2009) 5–13, https://doi.org/10.1016/j.jcat.2009.07.005.
[98] E.M. Sadovskaya, A.S. Bobin, V.V. Skazka, Isotopic transient analysis of oxygen exchange over oxides, Chem. Eng. J. 348 (2018) 1025–1036, https://doi.org/10.1016/j.cej.2018.05.027.
[99] A.M. Efstathiou, S.Y. Christou, Investigation of the Oxygen Storage and Release Kinetics of Model and Commercial Three-Way Catalytic Materials By Transient Techniques. Catalysis by Ceria and Related Materials 2nd ed., 12, Imperial College Press, 2013, pp. 139–221, https://doi.org/10.1142/9781848169647_0003.
[100] S. Ackermann, J.R. Scheffe, A. Steinfeld, Diffusion of oxygen in ceria at elevated temperatures and its application to H_2O/CO_2 splitting thermochemical redox cycles, J. Phys. Chem. C 118 (2014) 5216–5225, https://doi.org/10.1021/jp500755t.
[101] Y. Ding, Y. Choi, Y. Chen, K.C. Pradel, M. Liu, Z.L. Wang, Quantitative nanoscale tracking of oxygen vacancy diffusion inside single ceria grains by in situ transmission electron microscopy, Mater. Today 38 (2020) 24–34, https://doi.org/10.1016/j.mattod.2020.04.006.
[102] A.W. Sakti, C.-P. Chou, Y. Nishimura, H. Nakai, Is oxygen diffusion faster in bulk CeO_2 or on a (111)-CeO_2 surface? A theoretical study, Chem. Lett. 50 (2021) 568–571, https://doi.org/10.1246/cl.200895.
[103] X. Liu, K. Zhou, L. Wang, B. Wang, Y. Li, Oxygen vacancy clusters promoting reducibility and activity of ceria nanorods, J. Am. Chem. Soc. 131 (2009) 3140–3141, https://doi.org/10.1021/ja808433d.
[104] Z. Ou, J. Ran, H. Qiu, X. Huang, C. Qin, Uncovering the effect of surface basicity on the carbon deposition of Ni/CeO_2 catalyst modified by oxides in DRM, Fuel 335 (2023) 126994, https://doi.org/10.1016/j.fuel.2022.126994.
[105] Z. Ni, X. Djitcheu, X. Gao, J. Wang, H. Liu, Q. Zhang, Effect of preparation methods of CeO_2 on the properties and performance of Ni/CeO_2 in CO_2 reforming of CH_4, Sci. Rep. 12 (2022) 5344, https://doi.org/10.1038/s41598-022-09291-w.
[106] H.X. Mai, L.D. Sun, Y.W. Zhang, R. Si, W. Feng, H.P. Zhang, H.C. Liu, C.H. Yan, Shape-selective synthesis and oxygen storage behavior of ceria nanopolyhedra, nanorods, and nanocubes, J. Phys. Chem. B 109 (2005) 24380–24385, https://doi.org/10.1021/jp055584b.
[107] L. He, Y. Ren, Y. Fu, B. Yue, S.C.E. Tsang, H. He, Morphology-dependent catalytic activity of Ru/CeO_2 in dry reforming of methane, Molecules 24 (2019), https://doi.org/10.3390/molecules24030526.
[108] M.A. Vasiliades, C.M. Damaskinos, K.K. Kyprianou, M. Kollia, A.M. Efstathiou, The effect of Pt on the carbon pathways in the dry reforming of methane over Ni-Pt/$Ce_{0.8}Pr_{0.2}O_{2-\delta}$ catalyst, Catal. Today 355 (2020) 788–803, https://doi.org/10.1016/j.cattod.2019.04.022.
[109] Y.L. Zhang, X.J. Liu, Z. Sun, Z. An, Dynamics of exciton transfer in coupled polymer chains, J. Chem. Phys. 138 (2013) 174906, https://doi.org/10.1063/1.4803163.
[110] T.J. Huang, H.J. Lin, T.C. Yu, A comparison of oxygen-vacancy effect on activity behaviors of carbon dioxide and steam reforming of methane over supported nickel catalysts, Catal. Lett. 105 (2005) 239–247, https://doi.org/10.1007/s10562-005-8697-2.
[111] N. Köpfle, T. Götsch, M. Grünbacher, E.A. Carbonio, M. Hävecker, A. Knop-Gericke, L. Schlicker, A. Doran, D. Kober, A. Gurlo, S. Penner, B. Klötzer, Zirconium-Assisted Activation of Palladium To Boost Syngas Production by Methane Dry Reforming, Angew. Chem. Int. Ed. 57 (2018) 14613–14618, https://doi.org/10.1002/anie.201807463.
[112] W. Chen, R. Ran, D. Weng, X. Wu, J. Zhong, S. Han, Influence of morphology on basicity of CeO_2 and its use in 2-chloroethyl ethyl sulfide degradation, J. Rare Earths 35 (2017) 970–976, https://doi.org/10.1016/S1002-0721(17)61001-9.
[113] D. Shen, Z. Li, J. Shan, G. Yu, X. Wang, Y. Zhang, C. Liu, S. Lyu, J. Li, L. Li, Synergistic Pt-CeO_2 interface boosting low temperature dry reforming of methane, Appl. Catal. B Environ. 318 (2022) 121809, https://doi.org/10.1016/j.apcatb.2022.121809.
[114] Y. Bai, K. Sun, J. Wu, M. Zhang, S. Zhao, Y.D. Kim, Y. Liu, J. Gao, Z. Liu, Z. Peng, The Ga-promoted Ni/CeO_2 catalysts for dry reforming of methane with high stability induced by the enhanced CO_2 activation, Mol. Catal. 530 (2022) 112577, https://doi.org/10.1016/j.mcat.2022.112577.
[115] Z. Wu, A.K.P. Mann, M. Li, S.H. Overbury, Spectroscopic Investigation of Surface-Dependent Acid-Base Property of Ceria Nanoshapes, J. Phys. Chem. C. 119 (2015) 7340–7350, https://doi.org/10.1021/acs.jpcs.5b00859.
[116] Z. Tan, G. Li, H.-L. Chou, Y. Li, X. Yi, A.H. Mahadi, A. Zheng, S.C. Edman Tsang, Y.-K. Peng, Differentiating Surface Ce Species among CeO_2 Facets by Solid-State NMR for Catalytic Correlation, ACS Catal. 10 (2020) 4003–4011, https://doi.org/10.1021/acscatal.0c00014.

[117] M.A.A. Aziz, A.A. Jalil, S. Wongsakulphasatch, D.V.N. Vo, Understanding the role of surface basic sites of catalysts in CO_2 activation in dry reforming of methane: a short review, Catal. Sci. Technol. 10 (2020) 35–45, https://doi.org/10.1039/c9cy01519a.

[118] C. Papadopoulou, H. Matralis, X. Verykios, Utilization of biogas as a renewable carbon source: Dry reforming of methane, in: L. Guczi, A. Erdôhelyi (Eds.), Catal. Altern. Energy Gener., Springer, New York, 2012, pp. 57–127, https://doi.org/10.1007/978-1-4614-0344-9_3.

[119] N.A.K. Aramouni, J.G. Touma, B.A. Tarboush, J. Zeaiter, M.N. Ahmad, Catalyst design for dry reforming of methane: Analysis review, Renew. Sustain. Energy Rev. 82 (2018) 2570–2585, https://doi.org/10.1016/j.rser.2017.09.076.

[120] M.M. Makri, M.A. Vasiliades, K.C. Petallidou, A.M. Efstathiou, Effect of support composition on the origin and reactivity of carbon formed during dry reforming of methane over 5 wt% $Ni/Ce_{1-x}M_xO_{2-\delta}$ ($M = Zr^{4+}$, Pr^{3+}) catalysts, Catal. Today 259 (2016) 150–164, https://doi.org/10.1016/j.cattod.2015.06.010.

[121] M.A. Vasiliades, P. Djinović, A. Pintar, J. Kovač, A.M. Efstathiou, The effect of CeO_2-ZrO_2 structural differences on the origin and reactivity of carbon formed during methane dry reforming over $NiCo/CeO_2$-ZrO_2 catalysts studied by transient techniques, Catal. Sci. Technol. 7 (2017) 5422–5434, https://doi.org/10.1039/c7cy01009e.

[122] M.A. Vasiliades, C.M. Damaskinos, P. Djinović, A. Pintar, A.M. Efstathiou, A transient isotopic study for investigating important design parameters of $NiCo/Ce_{0.75}Zr_{0.25}O_{2-\delta}$ catalyst for the dry reforming of methane, Catal. Commun. 178 (2023) 106674, https://doi.org/10.1016/j.catcom.2023.106674.

[123] N. Wang, W. Qian, W. Chu, F. Wei, Crystal-plane effect of nanoscale CeO_2 on the catalytic performance of Ni/CeO_2 catalysts for methane dry reforming, Catal. Sci. Technol. 6 (2016) 3594–3605, https://doi.org/10.1039/C5CY01790D.

[124] P. Djinović, A. Pintar, Stable and selective syngas production from dry CH_4-CO_2 streams over supported bimetallic transition metal catalysts, Appl. Catal. B Environ. 206 (2017) 675–682, https://doi.org/10.1016/j.apcatb.2017.01.064.

[125] W. Xu, Z. Liu, A.C. Johnston-Peck, S.D. Senanayake, G. Zhou, D. Stacchiola, E. A. Stach, J.A. Rodriguez, Steam Reforming of Ethanol on Ni/CeO_2: Reaction Pathway and Interaction between Ni and the CeO_2 Support, ACS Catal. 3 (2013) 975–984, https://doi.org/10.1021/cs4000969.

[126] Z. Li, K. Werner, K. Qian, R. You, A. Plucienik, A. Jia, L. Wu, L. Zhang, H. Pan, H. Kuhlenbeck, S. Shaikhutdinov, W. Huang, H.-J. Freund, Oxidation of reduced ceria by incorporation of hydrogen, Angew. Chem. Int. Ed. 58 (2019) 14686–14693, https://doi.org/10.1002/anie.201907117.